https://doi.org/10.5194/egusphere-2026-5725
Preprint. Discussion started: 3 November 2026
© Author(s) 2026. CC BY 4.0 License.

Nuclear contamination limits $^{14}CH_4$ but not $^{14}CO_2$ source attribution in a five-year Swiss atmospheric monitoring network

Dylan Geissbühler[1,2,a], Thomas Laemmel[1,2], Stephan Henne[3], Dominik Brunner[3], Negar Haghipour[4], Philip Gautschi[4], Markus Leuenberger[2,5], Christophe Espic[1,2,b], Matthias Bantle[1], Heather Graven[6], Lukas Wacker[4], Sönke Szidat[1,2]

[1]Department of Chemistry, Biochemistry and Pharmaceutical Sciences, University of Bern, Bern, Switzerland
[2]Oeschger Centre for Climate Change Research, University of Bern, Bern, Switzerland
[3]Empa, Laboratory for Air Pollution/Environmental Technology, Dübendorf, Switzerland
[4]Laboratory for Ion Beam Physics, Department of Physics, ETH Zurich, Zürich, Switzerland
[5]Climate and Environmental Physics, University of Bern, Bern, Switzerland
[6]Department of Physics, Imperial College London, London, United Kingdom
[a]Now at Institute for Marine and Atmospheric research Utrecht (IMAU), Utrecht University, Utrecht, The Netherlands
[b]Now at MIRO Analytical AG, Wallisellen, Switzerland

Correspondence to: Dylan Geissbühler (d.c.geissbuhler@uu.nl)

Abstract. Radiocarbon (^{14}C) measurements of atmospheric CO_2 and CH_4 enable distinction between fossil and modern biogenic sources, providing critical constraints for emission inventories and mitigation efforts. We present multi-year, multi-site atmospheric $^{14}CO_2$ and $^{14}CH_4$ data from a monitoring network in Switzerland (2019–2023), combining fortnightly sampling at five boundary layer sites (4 rural and 1 urban) on the Swiss Plateau and the alpine background station Jungfraujoch with FLEXPART-COSMO atmospheric transport simulations based on Swiss and European emission inventories. Fossil CO_2 estimates showed expected spatial patterns, with highest values at the urban site and reasonable agreement with inventory-based simulations. Nuclear $\Delta(^{14}C, CO_2)$ contamination was negligible (+0.2 ± 0.4 ‰) and recent observations of Swiss ecosystem respiration $\Delta(^{14}C, CO_2)$ signature indicated that the respiration correction was also quite small. In contrast, $^{14}CH_4$ measurements revealed pervasive nuclear contamination that severely compromised fossil CH_4 source apportionment. Sporadic nuclear $^{14}CH_4$ releases could not be adequately resolved with monthly/quarterly emission data from nuclear power plant operators, leading to large model-observation mismatches and physically implausible fossil CH_4 estimates. This demonstrates a fundamental limitation of $^{14}CH_4$ for quantitative source attribution in nuclear-influenced regions. The contrasting success of $^{14}CO_2$ versus $^{14}CH_4$ underscores the need for tracer-specific strategies and highlights challenges posed by expanding nuclear infrastructure globally.

1 Introduction

Emissions of greenhouse gases (GHG) to the atmosphere, in particular of carbon dioxide (CO_2) and methane (CH_4), are the main contributors to climate change since the onset of the industrial revolution (Calvin et al., 2023). Monitoring and

https://doi.org/10.5194/egusphere-2026-5725
Preprint. Discussion started: 3 November 2026
© Author(s) 2026. CC BY 4.0 License.

attributing these emissions to specific sources (fossil fuel combustion, agriculture, land use change) is essential for effective climate mitigation policies. A variety of approaches have been developed for this purpose, ranging from bottom-up emission inventories to top-down methods combining atmospheric measurements with transport models. Top-down approaches rely on tracers to distinguish source types: auxiliary gases (e.g., CO, radon, SF_6) can identify pollution plumes or air mass origins, while isotopic measurements (e.g., $\delta(^{13}C)$, $\delta(^{2}H)$, $\Delta(^{14}C)$) enable direct differentiation between fossil and modern biogenic carbon sources (Levin et al., 1992, 2022; Miller et al., 2012).

Radiocarbon (^{14}C), a naturally occurring radioisotope with a half-life of 5700 ± 30 years (Kutschera, 2019), is produced in the stratosphere through cosmic ray interactions with ^{14}N and subsequently oxidized to $^{14}CO_2$, entering the carbon cycle via photosynthesis and ocean-atmosphere exchange (Schuur et al., 2016). Atmospheric ^{14}C levels were dramatically elevated by nuclear weapons testing in the 1950s-1960s, an effect known as the "bomb peak" (Graven et al., 2024; Hua et al., 2022). Additionally, ^{14}C is continuously released by the nuclear industry, primarily from nuclear power plants (NPPs) and nuclear fuel reprocessing plants (NFRPs) (Yim and Caron, 2006; Zazzeri et al., 2018).

Radiocarbon (^{14}C) enables source apportionment between fossil sources (such as coal, oil, natural gas), which are devoid of ^{14}C due to radioactive decay over millions of years, and modern sources (e.g., biomass, biogenic waste), which have ^{14}C signatures near contemporary atmospheric values. Combined with atmospheric transport modelling, $^{14}CO_2$ and $^{14}CH_4$ measurements provide top-down constraints on fossil emissions at scales ranging from individual facilities (Geissbühler et al., 2025; Turnbull et al., 2014) to urban regions (Graven et al., 2018; Turnbull et al., 2019; Zazzeri et al., 2023) and continental domains (Basu et al., 2020; Gómez-Ortiz et al., 2025). These constraints are increasingly used to validate bottom-up emission inventories and detect unreported fossil sources.

However, $^{14}CH_4$-based source apportionment faces a critical challenge from nuclear ^{14}C contamination. Nuclear ^{14}C, produced in reactors via $^{17}O(n,\alpha)^{14}C$, $^{14}N(n,p)^{14}C$, and $^{13}C(n,\gamma)^{14}C$ reactions, is released predominantly as gaseous emissions with speciation depending on reactor type: pressurized water reactors (PWRs, ≈60 % of global electrical production capacity) emit primarily $^{14}CH_4$ due to reducing coolant conditions, while boiling water reactors (BWRs, ≈ 24 %) and pressurized heavy-water reactors (PHWRs, ≈11 %) emit predominantly $^{14}CO_2$ (IAEA PRIS, 2026; Yim and Caron, 2006). Nuclear fuel reprocessing plants (*e.g.*, La Hague, Sellafield (until 2022)) are additional major $^{14}CO_2$ sources. Although global annual emissions (≈105 TBq $^{14}CO_2$ vs. ≈45 TBq $^{14}CH_4$ in 2016 (Zazzeri et al., 2018) are larger for $^{14}CO_2$, the atmospheric $^{14}CH_4/^{12}CH_4$ ratio is far more sensitive due to CH_4's about 200 times lower amount compared to CO_2. Early studies documented this challenge: measurements in the Netherlands showed values three times background levels even far from known sources, indicating long-range nuclear $^{14}CH_4$ transport (Eisma et al., 1994, 1995), while in London 3 of 7 samples were nuclear-contaminated (Zazzeri et al., 2023). Improved nuclear emission inventories and transport modelling remain critical needs for robust $^{14}CH_4$-based source apportionment (Fujita et al., 2025; Graven et al., 2019).

Switzerland, located in Western Europe, is dominated by two mountain ranges: the Alps in the south and the Jura mountains in the northwest, with most anthropogenic emissions occurring on the Swiss Plateau, a densely populated lowland corridor extending southwest-northeast from Lake Geneva to Lake Constance. Major urban centres on the Plateau include Zurich,

https://doi.org/10.5194/egusphere-2026-5725
Preprint. Discussion started: 3 November 2026
© Author(s) 2026. CC BY 4.0 License.

Geneva, Lausanne, Winterthur and Bern, while intensive agriculture dominates rural areas. In 2024, total greenhouse gas emissions were 39.8 Mt CO_2-eq (excluding Land Use, Land Use Change and Forestry, LULUCF), with fossil CO_2 (32.7 Mt) predominantly from energy and transport sectors, while CH_4 emissions originate primarily from agriculture (86 %), waste management (11 %) and fugitive emissions from fossil sources (1 %) (FOEN, 2026). While Switzerland's total greenhouse gas emissions have followed a downward trend since 1990 (−27.3 % excluding LULUCF; FOEN, (2026)), independent, top-down verification of these reported reductions remains essential, as bottom-up inventories can be subject to unaccounted, misreported, or slowly-updated emission sources. Radiocarbon provides such an independent constraint, enabling direct discrimination between fossil and modern-carbon sources of atmospheric CO_2 and CH_4 without reliance on activity data or emission factors. Three of Switzerland's four nuclear power plants operate on or near the Plateau: three pressurized water reactors (Gösgen, Beznau 1-2) and one boiling water reactor (Leibstadt). A fourth boiling water reactor at Mühleberg, was decommissioned in December 2019.

This study presents to our knowledge the first multi-year, multi-site atmospheric $^{14}CO_2$ and $^{14}CH_4$ data from a monitoring network in Switzerland (2019-2023), with fortnightly air sampling at five Swiss Plateau sites and the alpine background station Jungfraujoch. The JFJ observations were obtained within the same sampling campaign and have been published by Laemmel et al. (2026), who analysed their temporal evolution, the regional nuclear influence and the global atmospheric $^{14}CH_4$ signal; here, they serve as background and reference for the Plateau sites. The Plateau observations, their comparison with atmospheric transport simulations and the resulting fossil and nuclear source attribution are presented here for the first time. We use ^{14}C-based mass balance approaches to quantify fossil CO_2 and CH_4 contributions and compare them to expected contributions based on bottom-up inventories and FLEXPART-COSMO atmospheric transport simulations. We assess biospheric flux influences using an updated ecosystem respiration ^{14}C signature and evaluate nuclear ^{14}C contamination using a comprehensive European nuclear emission inventory. Our work aims to: (1) establish baseline atmospheric ^{14}C levels for Switzerland across contrasting site types (urban, rural, background), (2) test the viability of $^{14}CH_4$ for fossil source apportionment in a nuclear-influenced region, and (3) provide long-term constraints on Swiss fossil emissions for comparison with bottom-up inventories.

2 Material and methods

2.1 Observation sites

Air samples were collected at a total of six sites (Fig. 1). Five of them are located across the Swiss Plateau which constitutes most of the low-altitude flatlands of the country. The sampling sites are spread in the orientation of the Swiss Plateau, allowing for the capture and comparison of emission signals over the entire region. The Swiss Plateau is also the region where three, Gösgen (GSG), Beznau 1-2 (BEZ), and Mühleberg (MUH) (closed in 2019), out of the four Swiss nuclear plants in operation are located. Leibstadt (LEI), the fourth, is located on the outskirts of the Jura mountains close to the

https://doi.org/10.5194/egusphere-2026-5725
Preprint. Discussion started: 3 November 2026
© Author(s) 2026. CC BY 4.0 License.

border with Germany. Out of the five sites, four of them are tall tower rural sites and the fifth is an urban site, located in the
100 city of Bern.

Owing to its longest continuous measurement record among the network sites, the *Blosenbergturm* tall tower in Beromünster (BRM) serves as the main site of this study. The base of this decommissioned telecommunication tower is at 798 m above sea level (a.s.l.) and has been used extensively in the past for a diversity of atmospheric measurements and air sampling campaigns (Berhanu et al., 2016; Oney et al., 2015; Satar et al., 2016). The tower is fitted with sampling lines at five

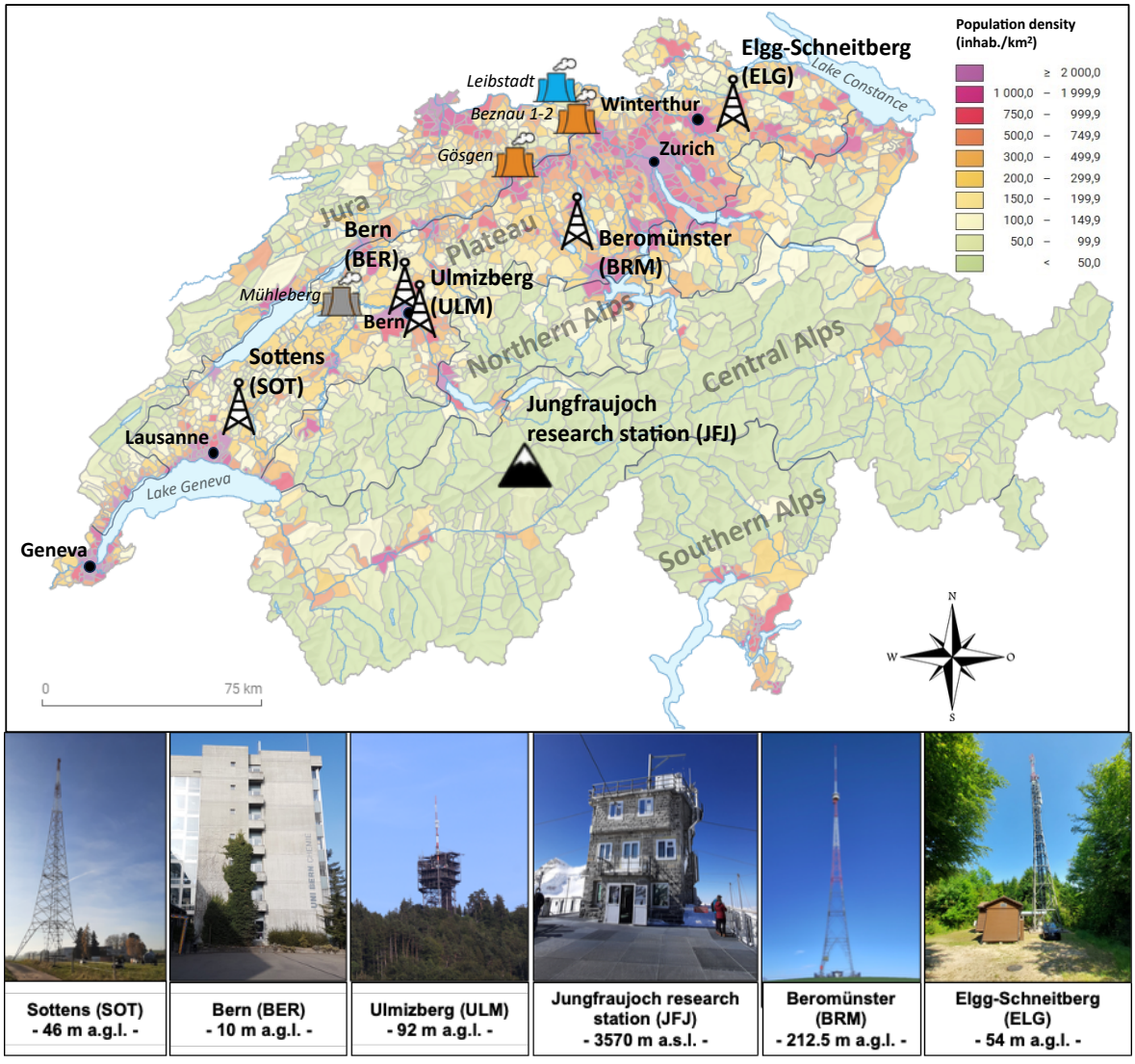


Figure 1: (Top) Map of Switzerland with its main ecoregions, cities and the population density in the background. Plateau sampling sites are indicated by white towers, the background alpine site Jungfraujoch is indicated as a mountain. NPP locations are indicated with cooling towers, BWR in blue, PWR in orange, decommissioned in grey. Map source: atlas.bfs.admin.ch. (Bottom) Pictures of all the sampling sites, with height above ground level (a.g.l.) of their respective sampling inlets and altitude above sea level (a.s.l.) for JFJ.

https://doi.org/10.5194/egusphere-2026-5725
Preprint. Discussion started: 3 November 2026
© Author(s) 2026. CC BY 4.0 License.

different heights, but samples were collected at the highest sampling height only (212.5 m a.g.l.).

The alpine background site is located at the High-Altitude Research Station Jungfraujoch (JFJ), with samples collected at an elevation of 3570 m a.s.l. This site is considered to be an atmospheric background location at the European scale, mostly unaffected by local emissions (Henne et al., 2010; Herrmann et al., 2015; Levin et al., 2022). The JFJ $^{14}CO_2$ and $^{14}CH_4$ observations used in this study are those published by Laemmel et al. (2026).

Sottens (SOT) is a 120 m tall tower, used for radio telecommunication until 2010, located in the western part of the Swiss Plateau at 776 m a.s.l. Its setting is rural and it has served as one of the atmospheric background locations in the Integrated Carbon Observatory System (ICOS)-Cities project since 2022 (Grange et al., 2024). The sampling line inlet used at SOT is at 46 m a.g.l. and is shared with the ICOS-Cities measurements.

Air sampling in Bern (BER) was conducted from the second floor of the Department for Chemistry, Biochemistry and Pharmaceutical Sciences of the University of Bern. For this, air was sampled using a line passing through the window of the lab, at about 10 m a.g.l. This site is an urban station, located in the metropolitan area of Bern which encompasses around 400'000 inhabitants. While the building is in a relatively densely inhabited neighbourhood, close to important traffic junctions, the immediate surroundings of the building have low traffic presence and no major fossil CO_2 sources (Van Der Laan et al., 2014).

Ulmizberg (ULM) is a 95 m tall telecommunication tower, situated on a 937 m hill, about 5 km south of the city of Bern; the inlet was placed on the tower mast at 92 m a.g.l. Finally, the Elgg-Schneitberg tower (ELG) is 64 m tall and is in a forested area of the eastern Swiss Plateau. It is about 10 km east of the city of Winterthur, which itself is between the larger city of Zurich and Lake Constance. The inlet elevation of the sampling line is 54 m a.g.l. More detailed information about each of the sites may be found in Table A1.

2.2 Air sampling procedure

A fortnightly sampling program originally started in July 2018 at the site BRM and was then extended to BER in October 2018 and to JFJ in December 2018. The site SOT joined the monitoring network later in June 2021 and the remaining sites ULM and ELG in March and May of 2023, respectively. For the sites on the Swiss Plateau (i.e., BER, BRM, ELG, SOT and ULM), air was originally sampled for varying durations, between 20 min and 1.5 h around the early afternoon, except for BER and BRM, which were initially sampled in the morning. From March 2021, air sampling at BER was conducted in the afternoon. From November 10th, 2022, the air sampling procedure was homogenized to take place for one hour, between 14:00 and 15:00 UTC, for all Swiss Plateau sites.

The sampling setup usually consisted of a membrane pump transferring air from the inlet located at a high position on the sampling structure via an aluminium/polyethylene (Al/PE) line (Synflex, Eaton, USA) into 120 to 220 L PE/Al/PE bags (Tesseraux Spezialverpackungen GmbH, Germany) and transported back to the lab for further processing. Both CH_4 and CO_2 were extracted from the same sample bag. Wet air was sampled until November 2021 at BER, JFJ and SOT (until

https://doi.org/10.5194/egusphere-2026-5725
Preprint. Discussion started: 3 November 2026
© Author(s) 2026. CC BY 4.0 License.

October 2022 at BRM), when we added a magnesium perchlorate ($Mg(ClO_4)_2$) dryer to chemically remove water vapour from the air before entering the bag. The specific features of air sampling for each site are presented below.

At BER, air was commonly sampled by a membrane pump (MZ 2C NT, Vacuubrand, Germany) which is also used in the setup to extract CH_4 and CO_2 for ^{14}C analysis. The sampled air was stored into its bag until further analysis, starting in March 2021; previously, air was generally sampled through the window of the laboratory and directly processed to separate the CH_4 and CO_2 fractions for ^{14}C analysis (c.f. section 2.3.2). At BRM, air sampling took place at the outlet of the flushing pump (617CD32, Gardner Denver, USA) of the 212.5 m sampling line. The high flow rate (≈ 10 L min^{-1}, at ambient conditions) of the pump explains the quick sampling time (17-21 min) until October 2022. From November 10th, 2022, only part of the outlet air was sampled using a by-pass and a mass flow controller (MassView MV-405, Bronkhorst, The Netherlands) to allow for a one-hour sampling at 3 L min^{-1} (at 0 °C and 1013.25 hPa). At the JFJ site, air sampling was performed in the early morning at the Sphinx terrasse of the research station using a membrane pump (N022AN.18, KNF Neuberger AG, Germany) until March 2023. In April 2023, the Jungfraujoch Air Sampling System (JASS) was installed under the roof of the research station allowing for an automated air collection (Laemmel et al., 2026). Using this system, each sample was collected during a two-week period, at nighttime (00:00 to 06:00 UTC), to constitute an integrated background air sample. At SOT, sampling was performed manually with a membrane pump (Laboport N816.1.KT.18, KNF Neuberger AG, Germany) using the shared ICOS-Cities sampling line going to 46 m. For this, a switching valve was installed allowing the diversion of the air flow around the ICOS-Cities CO_2 sensor. At ULM, the pump (PM34215-96, KNF Neuberger SAS, France) was activated in advance, and a valve connected to a timer allowed the operator to set the sampling time, at which the valve activates, filling the bag and then turns off one hour later. This was done because a single operator had to sample at two sites simultaneously. From November 1st, 2023, a remotely operated setup developed specifically for the collection of air samples at tall towers, the Monitoring Air Sampling System (MASS), was used at ULM; it was based on an auto-regulating membrane pump maintaining a predefined airflow through a microcontroller (NMP830 Demo-Kit SmartPump, KNF Micro AG, Switzerland). It allowed the operator to attach a sampling bag in advance, remotely decide on the sampling time and duration, and the system automatically sampled air at a fixed rate. The whole system was contained within a metal box, in which the upper part houses the valves and controls, and the bottom part accommodates a 100 L bag in a protected way (Fig. A1). At the ELG site, sampling was conducted manually using a membrane pump (Laboport N96, KNF Neuberger AG, Germany).

2.3 Measurements

2.3.1 Initial CO_2 and CH_4 measurements

In situ continuous atmospheric GHG measurements at the BRM tall tower started in November 2012 in the framework of the CarboCount-CH project (Berhanu et al., 2016; Oney et al., 2015; Satar et al., 2016). There, atmospheric CO_2 and CH_4 have

https://doi.org/10.5194/egusphere-2026-5725
Preprint. Discussion started: 3 November 2026
© Author(s) 2026. CC BY 4.0 License.

been continuously measured via Cavity Ring-Down Spectroscopy (CRDS) (G2401 Gas Concentration Analyzer, Picarro, Inc., USA), each of the five sampling heights being measured in turn for 20 min. Since 2013, samples for $^{14}CO_2$ analysis have also been collected there regularly (Berhanu et al., 2017).

The JFJ station holds the status of an ICOS Class 1 Atmosphere Station since May 2018. There, in situ atmospheric CO_2 and CH_4 are continuously measured via CRDS (G2401 Gas Concentration Analyzer, Picarro, Inc., USA) and available online via the ICOS Carbon Portal (Emmenegger et al., 2024a). As part of the Zurich network for the ICOS-Cities project (Grange et al., 2024), CO_2 has been measured in situ at SOT since May 2021 with a Senseair HPP CO_2 sensor (High-Performance Platform, Senseair AB, Sweden).

For the remaining sampling stations, no continuous in situ GHG measurements are available (BER, ELG, SOT for CH_4, and ULM). CO_2 and CH_4 mole fractions of the air samples were determined in the laboratory using a CRDS analyser (G2401 Gas Concentration Analyzer, Picarro, Inc., USA) calibrated with three reference bottles (379.2, 418.4, and 458.6 µmol mol^{-1} for CO_2 and 1861, 1956, and 2207 nmol mol^{-1} for CH_4; values provided by the Institute for Climate and Environmental Physics, University of Bern, see Berhanu et al., 2016) from October 2021 onwards. Air samples from the sites BRM, JFJ and SOT were also measured with this device to compare the mole fractions with the in-situ values; this was done for quality control and to identify possible sampling issues, especially leaking or contaminated sampling bags. Some bags were found to lose their quality after around 6 months and were thus replaced. Since October 2022, the mole fraction of CO_2 samples transferred to 5 L bags was additionally measured using a CRDS analyser (G2131-i, Picarro Inc., USA) at ETH Zurich (ETHZ). Each measurement took place for at least 5 min of stable conditions, from which the average CO_2 mole fraction was calculated. The standards, filled into the same 5 L bags, were also measured to assess any change in CO_2 mole fraction during the sample transfer and conservation process, as well as to have a CO_2 mole fraction as representative as possible of the sample analysed for $^{14}CO_2$.

2.3.2 Radiocarbon analyses at LARA

We use the $^{14}CH_4$-$^{14}CO_2$ extraction and analysis setup at the Laboratory for the Analysis of Radiocarbon with AMS (Accelerator Mass Spectrometry) (LARA) in Bern that is described in detail in Espic et al. (2019). From an initial volume of 60 L, air is pumped successively through three traps cooled down with liquid nitrogen, a preconcentration step allows to preserve the whole amount of CH_4 contained in the initial 60 L of air while trapping or pumping away the main other gas species, especially nitrogen, oxygen, and argon; CO_2 is quantitatively trapped in the first trap and can be collected separately. After that, the remaining gas sample volume is about 10 mL, small enough to inject it through a gas chromatograph (GC, 7890B, Agilent, USA; ShinCarbon packed column; thermal conductivity detector, He as carrier gas) to purify the sample and isolate quantitatively CH_4 from remaining CO and CO_2 present in trace quantities due to different eluting times in the GC. Downstream of the GC, CH_4 is combusted into CO_2 in a flow oven at 950 °C using copper oxide wires. The CH_4-derived CO_2 (about 60 to 70 µg of carbon, µg C) is finally cryogenically transferred into glass ampoules (OD = 4 mm) and sealed for ^{14}C gas measurements. At the end of the whole CH_4 extraction procedure, the CO_2 of the sample held in the first trap is

https://doi.org/10.5194/egusphere-2026-5725
Preprint. Discussion started: 3 November 2026
© Author(s) 2026. CC BY 4.0 License.

recovered by cryogenically transferring it into a ≈55 mL glass flask. The carbon mass associated with the recovered CO_2 is higher than 1 mg C, enabling a graphitization step in which the gaseous CO_2 is transformed into graphite using a dedicated automated graphitization equipment (AGE, Ionplus AG, Switzerland) (Wacker et al., 2010b).

Gaseous CH_4-derived CO_2 samples and graphite CO_2 samples were measured for ^{14}C either at LARA or at the Laboratory for Ion Beam Physics (LIP), ETHZ. Both laboratories use the same type of accelerator mass spectrometer (AMS), the MIni CArbon DAting System (MICADAS, Ionplus AG, Switzerland), equipped with a gas ion source (Ruff et al., 2007; Synal et al., 2007). At LARA, glass ampoules were cracked in a dedicated gas interface system (GIS, Wacker et al., 2013), and the CH_4-derived CO_2 was mixed with He to a ratio of ≈ 5 %, transferred into a syringe, and then fed into the ion source using a constant gas flow. Graphite samples were directly introduced in the MICADAS. For both types of samples, raw $^{14}C/^{12}C$ as well as $^{13}C/^{12}C$ ratios were converted into $\Delta(^{14}C)$ and $\delta(^{13}C)$ values respectively by performing a blank subtraction, a standard normalization and a correction for isotope fractionation (only for $\Delta(^{14}C)$) using ^{14}C-free CO_2 and CO_2 produced from the primary standard Oxalic Acid II (OxII, NIST SRM 4990C), respectively (Stuiver and Polach, 1977). For the gas measurements, both the blank and OxII standards came from gas bottles directly (5 % CO_2 in helium) connected to the GIS. For the graphite measurements, the pure blank and standard CO_2 underwent the same sample preparation as the real CO_2 samples and were measured with them in the same magazine. The final data evaluation was done using the tool BATS (Wacker et al., 2010b). Typical measurement precision is ≤ ±12 ‰ for $^{14}CH_4$ and ≤ ±3 ‰ for $^{14}CO_2$ (Espic et al., 2019).

2.3.3 Radiocarbon analyses at LIP

In addition to the analyses at LARA, whole-air samples were also processed and measured for $^{14}CO_2$ at the Laboratory for Ion Beam Physics (LIP), ETHZ, starting in October 2022. The 5 L air bag samples, that were subsampled from the 120 to 220 L bags, were graphitized using an in-house Air Loading Facility (ALF) coupled to an Automatized Graphitization Equipment (AGE3, ETHZ, Switzerland) (Gautschi, 2017; Wacker et al., 2010b). Graphite samples were then measured either on a MICADAS or a LEA (Low Energy AMS, ETHZ, Switzerland) (Ramsperger et al., 2023; Wacker et al., 2010c). For the graphitization using the ALF, CO_2 from a pressurised air bottle (PAB) was used as a process reference and process blanks came from a $^{14}CO_2$-free air bottle. OxII and blanks were prepared from solid material using an Elemental Analyser (vario EL cube, Elementar, Germany) connected to an AGE graphitization system. Additionally, due to the limited availability of the LARA AMS in some periods, CH_4-derived CO_2 gas samples have also been measured at LIP, using a similar procedure to LARA. Typical measurement precision at LIP is < 2 ‰ for CO_2 samples and 12 ‰ for CH_4. Based on the close intercomparison of $\Delta(^{14}C, CO_2)$ values between the LARA and LIP laboratories that only showed a mean offset of 0.8 ‰ (Fig. A2), both datasets were merged without any supplementary corrections.

https://doi.org/10.5194/egusphere-2026-5725
Preprint. Discussion started: 3 November 2026
© Author(s) 2026. CC BY 4.0 License.

2.4 Atmospheric modelling of $^{14}CO_2$ and $^{14}CH_4$

2.4.1 Transport model

The Lagrangian particle dispersion model (LPDM) FLEXible PARTicle (FLEXPART) was used to simulate CO_2 and CH_4 mole fractions and $\Delta(^{14}C, CO_2)$ and $\Delta(^{14}C, CH_4)$ at the sampling sites and times (Pisso et al., 2019), operated in time-reversed, receptor-oriented mode. FLEXPART was driven by the meteorological fields from two Eulerian numerical weather prediction (NWP) models: the limited-area NWP model COSMO-1 of MeteoSwiss and the Integrated Forecasting System (IFS) of the European Centre for Medium-Range Weather Forecasts (ECMWF) beyond the COSMO-1 model domain (Katharopoulos et al., 2022). The COSMO-1 product has a high spatial resolution of 1 km × 1 km and is based on a Local Ensemble Transform Kalman filter assimilation of meteorological variables, resulting in high temporal resolution (1 hour) analysis fields for the Alpine domain (approximately 0-17°E, 42-50°N). High-resolution (HRES) IFS is the operational global NWP model of ECMWF (Malardel et al., 2016). Hourly model fields were available for FLEXPART at 0.1° × 0.1° horizontal resolution for Europe.

FLEXPART-COSMO was used in previous atmospheric studies including for verification of the Swiss CH_4 emission inventory (Henne et al., 2016), the simulation of CH_4, $\delta(^{13}C,CH_4)$ and $\delta(^{2}D,CH_4)$ at a tall tower in the Netherlands (Röckmann et al., 2016), simulation of the influence of nuclear ^{14}C emissions on $\Delta(^{14}C,CO_2)$ at the BRM tower (Berhanu et al., 2017), analysis of CO_2 and $\delta(^{13}C, CO_2)$ at the JFJ station (Pieber et al., 2022) and estimation of the emission of several F-gases in Switzerland (Katharopoulos et al., 2023). Here, the model was operated similarly to the description in Katharopoulos et al., (2023), releasing 50'000 model particles in 3-hourly intervals at the location of the observations and tracking these particles backward in time for 10 days. Particles that leave the limited COSMO domain are handed over to FLEXPART-IFS.

2.4.2 Regional CO_2 and CH_4 fluxes

To simulate receptor mole fractions, spatially distributed flux estimates are required. For this study, fluxes were taken from two sources. Swiss CO_2 and CH_4 anthropogenic fluxes were based on the Meteotest EKAT inventory, representing the spatial distribution of 43 emission groups at a 100 m × 100 m spatial resolution (Heldstab et al., 2021). CO_2 and CH_4 anthropogenic fluxes for the surrounding European countries were based on the TNO-CAMS v.4.2 product (Kuenen et al., 2022). It provides a spatial distribution of 15 emission groups at a resolution of 0.1° × 0.05°. We merged these two inventories by replacing TNO fluxes by Meteotest fluxes in Switzerland and by aggregating to six flux sectors depending on expected ^{14}C isotopic source signatures (CO_2: transport, fossil (*i.e.*, fuel use other than transport and heating), heating, wood burning, cement production, and waste (*i.e.*, incineration); CH_4: transport, fossil (*i.e.*, natural gas), wood burning, heating, cement production, and biogenic (agriculture, waste management)) (see Table B1). Concerning the anthropogenic CO_2 fluxes, time profiles were used to modulate the strength of the fluxes according to the hour of day, the day of week and the

https://doi.org/10.5194/egusphere-2026-5725
Preprint. Discussion started: 3 November 2026
© Author(s) 2026. CC BY 4.0 License.

month of year (Jähn et al., 2020). No time profiles were applied to CH_4 sources, as smaller variations in time are expected from the dominating agricultural source.

Natural biogenic CH_4 fluxes (*e.g.,* from wetlands) were not applied as they are considered to be a minor contributor in Switzerland (Hiller et al., 2014). Regional ecosystem CO_2 fluxes were based on the Vegetation Photosynthesis and Respiration Model (VPRM) (Mahadevan et al., 2008). Underlying parameters are specific for seven vegetation types (VTs) including (1) evergreen forest, (2) deciduous forest, (3) mixed forest, (4) shrubland, (5) savanna (not present in Europe), (6) cropland, and (7) grassland. Although the fluxes are generated based on the individual VTs, ecosystem respiration ($CO_{2,resp}$), ecosystem uptake (also called gross ecosystem exchange (GEE) and thus abbreviated $CO_{2,gee}$), and net ecosystem exchange (NEE) ($CO_{2,nee} = CO_{2,gee} - CO_{2,resp}$) are provided only as a 3-hourly total over all VTs. More details about the implementation of VPRM can be found in Pieber et al. (2022).

2.4.3. $^{14}CO_2$ and $^{14}CH_4$ signatures

On the edges of the European model domain, we assigned background $\Delta(^{14}C, CH_4)$ and $\Delta(^{14}C, CO_2)$ values based on ICOS two-week integrated measurements at JFJ over the five modelling years (2019 – 2023) (Emmenegger et al., 2024b). For $\Delta(^{14}C, CO_2)$, background was computed monthly, which declined steadily on a yearly basis, from +2 ‰ in 2019 to −8 ‰ in 2023 (−0.5 ‰ in 2020, −5 ‰ in both 2021 and 2022). The yearly $\Delta(^{14}C, CH_4)$ values (used as such because of larger variations in fortnightly data) were: 363 ‰ in 2019, 395 ‰ in 2020, 386 ‰ in 2021, 372 ‰ in 2022 and 377 ‰ in 2023 (see Table 1 in Laemmel et al., (2026)). The sensitivity of the results to the background definition, including the nuclear influence at JFJ and the change of the JFJ sampling protocol in April 2023, is assessed in Appendix C (Table C1). The $\Delta(^{14}C)$ values assigned to each emission group were gathered from the most recent available literature and updated as such: a $\Delta(^{14}C)$ value of −1000 ‰ (for CO_2 and CH_4) is assigned to the fossil emission group; fossil CH_4 emissions mainly correspond to leaks in the gas distribution network, while fossil CO_2 emissions mainly come from energy production, road transportation, and industrial processes (FOEN, 2024; SwissPRTR, 2024). The biospheric CO_2 flux signatures (GEE and respiration) and the associated flux correction are described in detail in Section 2.4.4.

A $\Delta(^{14}C)$ value of −940 ‰ was assigned to the heating emission group (private household and industry sectors); a fraction of 6 % biogas in the natural gas mix (Gazenergie-Verband der Schweiz, 2023) was assumed. A similar $\Delta(^{14}C)$ value of −950 ‰ was assigned to the transport emission group (including road and off-road transport, shipping and aviation); we assumed here a fraction of 5 % biodiesel (Verband Biofuels Schweiz, 2025). A $\Delta(^{14}C)$ value of −850 ‰ was assigned to the cement emission group; we assumed here a fraction of 15 % of non-fossil carbon emissions based on national fuel consumption in the cement industry and a recent study (cemsuisse, 2024; Geissbühler et al., 2025). For waste incineration, a $\Delta(^{14}C)$ value of −500 ‰ was chosen based on the work of Mohn et al. (2012). A $\Delta(^{14}C)$ value of +15 ‰ was assigned to the wood burning emission group (Mohn et al., 2008).

For CH_4, agricultural (enteric fermentation and manure management) and landfill/wastewater-derived methane were combined into a single biogenic flux, assigned a $\Delta(^{14}C)$ value of −9 ‰ based on the low-land grassland soil-respiration

https://doi.org/10.5194/egusphere-2026-5725
Preprint. Discussion started: 3 November 2026
© Author(s) 2026. CC BY 4.0 License.

signature (Minich et al. (2026); see Table B1), reflecting that Swiss livestock agriculture and associated waste streams are concentrated on lowland grassland and cropland. A $\Delta(^{14}C)$ value of +15 ‰ was assigned to the wood burning emission group (Geissbühler et al., 2025; Mohn et al., 2012).

2.4.4. Biospheric respiration correction

Initial simulations underestimated afternoon CO_2 mole fractions during summer months at BRM. Because the ^{14}C sampling window falls within the 12:00–15:00 UTC bin, we restricted the correction to this window only, rather than to the full diurnal cycle, to avoid fitting to times of day not represented by the actual ^{14}C samples. We applied a least-squares optimization to the simulated ecosystem respiration flux alone, using BRM's 12:00–15:00 UTC CO_2 data from 2018–2023; gross ecosystem exchange (GEE) was held fixed (factor = 1), since GEE removes ambient-composition air and is not expected to bias the fit. The optimization was performed using the R (v.4.4.2) (R Core Team, 2024) optim function with the "L-BFGS-B" method (Byrd et al., 1995), with a respiration correction factor derived separately for each season and year (summer: 01.04–01.10; winter: 01.10–01.04). Resulting factors ranged from 1.48 to 1.72 in summer and from 0.63 to 1.24 in winter (Table D1), consistently above 1 in summer and closer to 1 in winter. The resulting BRM-derived factors were applied to the 12:00–15:00 UTC data at all six sites, for both seasons. This correction modestly improved the CO_2 mole fraction fit at BRM, where it was calibrated (R^2 increased in most season-years; Table D1), but did not measurably influence the simulated–observed $\Delta(^{14}C, CO_2)$ agreement at any other site and did not consistently transfer to the other Plateau sites.

Concurrently, an updated $\Delta(^{14}C)$ signature of ecosystem respiration was derived from Minich et al. (2026), who measured soil-respiration $\Delta(^{14}C)$ across 16 sites in Switzerland spanning forests, croplands, and temperate and alpine grasslands. Site-level measurements were averaged into five Swiss land-use classes and combined into a single national signature by weighting each class by both its areal extent (Swiss land-cover statistics; FSO, 2026) and its respiration rate (Minich et al., 2026) (summer and winter values weighted separately), so that land-use types with higher respiration flux contribute proportionally more to the combined signature than area alone would suggest (Tables B2 and B3). Forest area was further split into conifer and deciduous/mixed stands (62 %/38 %; Swiss National Forest Inventory), each carrying its own measured signature and respiration rate. This flux-weighted combination yields a respiration signature of −5.3 ± 1.6 ‰, used throughout this study in place of a previously assumed value of +80 ‰ for simulations in the UK (Wenger et al., 2019).

2.4.5. Nuclear $^{14}CH_4$ and $^{14}CO_2$ emissions

Nuclear $^{14}CH_4$ and $^{14}CO_2$ emissions from nuclear facilities (NPPs and NFRPs) located in Europe were taken from the inventory of Laemmel et al. (2025). This dataset contains monthly ^{14}C emissions of the Swiss NPPs Gösgen and Leibstadt and of the NFRP La Hague (France) which is the strongest point source of $^{14}CO_2$ worldwide. It also contains quarterly ^{14}C emissions of the NPPs located in the neighbouring countries France and Germany. In addition to these published values, monthly emission values were also available for the Paks NPP, but annual values were taken for all other NPPs. Monthly, quarterly and annual $^{14}CO_2$ and $^{14}CH_4$ emission values were converted into 3-hour emission values assuming constant

https://doi.org/10.5194/egusphere-2026-5725
Preprint. Discussion started: 3 November 2026
© Author(s) 2026. CC BY 4.0 License.

emission rate over the corresponding reported periods. The implementation of this nuclear correction is described more details in Laemmel et al. 2026.

3. Results

3.1. Measured mole fractions and $\Delta(^{14}C)$ values

3.1.1. Measured CH_4 and $\Delta(^{14}C, CH_4)$

CH_4 mole fractions were generally lower at JFJ than at the five low-elevation sites (Fig. 2A), these sites being located on the Swiss Plateau and thus closer to CH_4 sources. An increasing CH_4 trend is visible at JFJ between 2019 and 2023: from an annual mean of 1930 nmol mol^{-1} in 2019, the CH_4 mole fraction reached an annual value of 1985 nmol mol^{-1} in 2023 (Emmenegger et al., 2025).

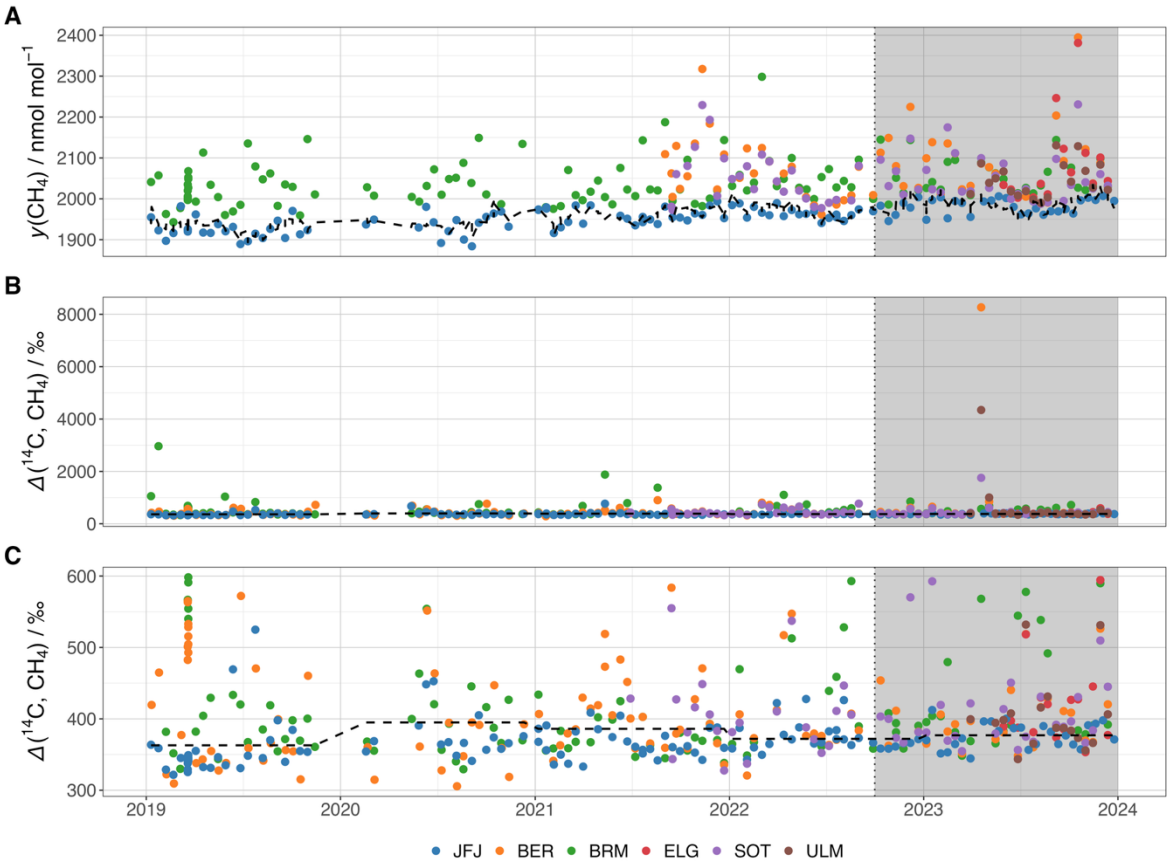


Figure 2: (A) CH_4 mole fractions and (B) $\Delta(^{14}C, CH_4)$ values for all the sampling sites between 2019 and 2023. The exceptionally high $\Delta(^{14}C, CH_4)$ values measured on April 19th, 2023, makes the data visualization challenging for data clarity, (C) is a zoom of subplot (B) between 300 and 600 ‰. All subplots show the background values used for the simulations as a dashed line. The shaded area (from November 2022) shows the period from which the sampling was homogenized between plateau sites (14:00 – 15:00 UTC).

https://doi.org/10.5194/egusphere-2026-5725
Preprint. Discussion started: 3 November 2026
© Author(s) 2026. CC BY 4.0 License.

Over the five sampling years (2019-2023), about 460 $^{14}CH_4$ measurements across all six sites were made (Fig. 2B); exceptionally high values were measured on April 19th, 2023, at the BER, ULM and SOT sites ($\Delta(^{14}C, CH_4)$ values up to 8266, 4345 and 2963 ‰, respectively. This is a more than 20 times higher ^{14}C excess than the commonly assumed background values of 340-350 ‰ (Graven et al., 2019; Zazzeri et al., 2018). About 62 % of all $\Delta(^{14}C, CH_4)$ values were lower than 400 ‰, about 83 % lower than 500 ‰ and about 90 % lower than 600 ‰ (Fig. 2C). At JFJ, $\Delta(^{14}C, CH_4)$ values are fairly constant with an annual average value of 363 ± 48 ‰ in 2019 and 377 ± 17 ‰ in 2023 (Laemmel et al., 2026), showing no significant difference within a 2σ uncertainty threshold. From April 2023, JFJ samples were collected as two-week integrated nighttime samples via the automated JASS system (Section 2.2), replacing manual grab samples; the resulting reduction in sampling variability is discussed in detail in (Laemmel et al., 2026). $\Delta(^{14}C, CH_4)$ values at JFJ are commonly lower than at the low-elevation sites indicating a ubiquitous influence of nuclear $^{14}CH_4$ emissions at these sites compared to JFJ. As described in Laemmel et al. (2026), JFJ is also subject to non-negligible nuclear ^{14}C influence from European nuclear power plants, mainly for $^{14}CH_4$ (+7 ± 9 ‰ average between 2019–2023). These values are based on samples filtered using joint radon (Rn) measurements, which serve as a tracer of continental boundary-layer influence at this high-altitude site, retaining only periods representative of background air. Some $\Delta(^{14}C, CH_4)$ values at the urban site BER before March 2021 have been lower than the values at JFJ, indicating a larger fossil CH_4 influence; this can be explained by the early sampling times during that period which could have collected air in which CH_4 from local fossil sources accumulated over the previous night, but generally BER was not shown to be influenced by CH_4 hot spots.

3.1.2. Measured CO_2 and $\Delta(^{14}C, CO_2)$

The background site JFJ generally shows lower CO_2 mole fractions than the sites located on the Swiss Plateau due to their proximity to anthropogenic CO_2 sources in that region (Fig. 3A). For JFJ, we see an increasing trend in CO2 mole fractions during the study period with values of 411.9 µmol mol^{-1} in 2019, 413.7 µmol mol^{-1} in 2020, 416.6 µmol mol^{-1} in 2021, 418.9 µmol mol^{-1} in 2022, and 421.1 µmol mol^{-1} in 2023 (Emmenegger et al., 2025). A seasonal cycle is visible on CO_2 mole fractions at all sites but is more pronounced at lowland sites. Lower CO_2 values from April to September (defined as "summer" in the analysis) are induced by increased photosynthetic uptake of CO_2 during the northern hemisphere vegetation growing season. Higher CO_2 values during the winter months (October – March) are caused by increased anthropogenic emissions, mainly due to heating sources, and reduced vertical mixing leading to the accumulation of emissions. In summer, the anthropogenic signal at lowland sites is compensated by the photosynthetic sink, bringing their CO_2 mole fractions close to background levels. Some days even show higher CO_2 mole fraction at JFJ, compared to some lowland sites (e.g., July 7th, 2022, August 9th, 2023) due to this effect. Concerning $\Delta(^{14}C, CO_2)$ values (Fig. 3B), general trends go in the opposite direction, with a decrease visible for the JFJ site, from −2.0 ± 3.8 ‰ in 2019 to −8.0 ± 2.3 ‰ in 2023, which is weaker than in previous decades (Levin et al., 2022). $\Delta(^{14}C, CO_2)$ values at JFJ are most of the time higher compared to lowland sites due to a higher contribution of fossil fuels there. During the summer months, the difference in $\Delta(^{14}C, CO_2)$ between Plateau sites and JFJ becomes smaller because of convection and the higher planetary boundary layer (PBL) in the warmer months so that

https://doi.org/10.5194/egusphere-2026-5725
Preprint. Discussion started: 3 November 2026
© Author(s) 2026. CC BY 4.0 License.

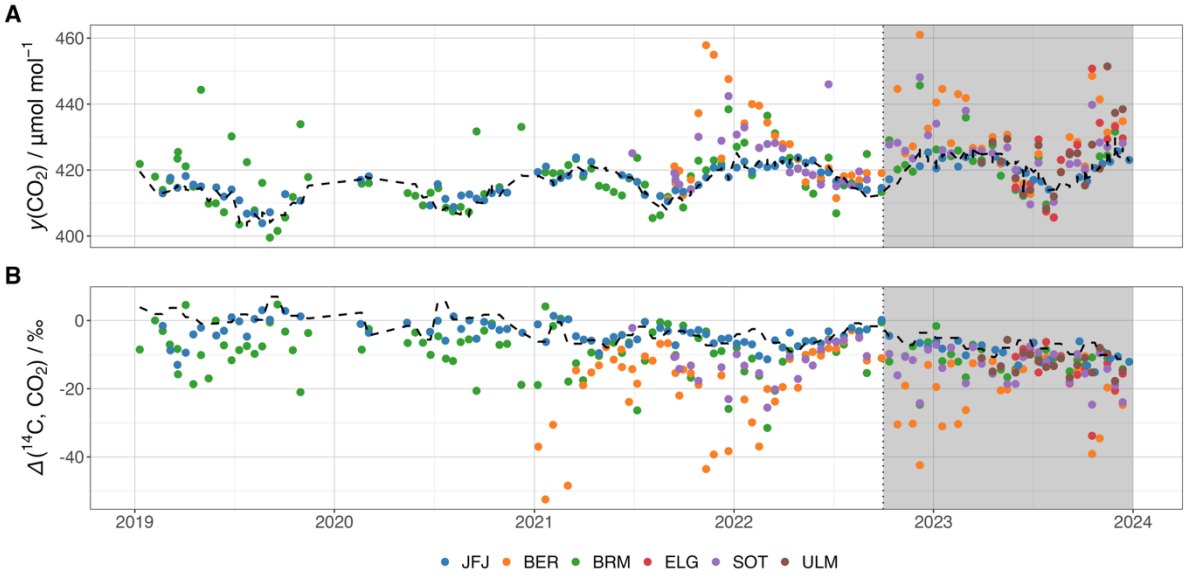


Figure 3: (A) CO_2 mole fractions and (B) $\Delta(^{14}C, CO_2)$ values for all the sampling sites between 2019 and 2023. CO_2 mole fraction values correspond to in situ measurements for the JFJ (ICOS network, Emmenegger et al., 2025), BRM and SOT (Grange et al., 2024; pers. comm. P. Rubli) sites, and sample measurements for the others. Background values are monthly-averaged JFJ values and were used as model background. The shaded area (from November 2022) shows the period from which the sampling was homogenized between plateau sites (14:00 – 15:00 UTC).

there is less local accumulation of fossil fuel CO_2. However, $\Delta(^{14}C, CO_2)$ is still typically lower in summer at the lowland sites compared to JFJ, such that the CO2 mole fraction reflects both the net uptake by vegetation and some local fossil fuel CO_2 present, which the $\Delta(^{14}C, CO_2)$ measurements can be used to quantify (Section 3.4).

3.1.3. $\Delta\Delta(^{14}C, CH_4)$ and $\Delta\Delta(^{14}C, CO_2)$ values across sites

Calculating the difference between $\Delta(^{14}C, CH_4)$ values from the lowland sites with simultaneous JFJ values ($\Delta\Delta(^{14}C, CH_4)$) shows positive values (Fig. 4A), with SOT having the highest median (27.9 ‰) and the other sites medians between 14.4 ‰ (BER) and 20.3 ‰ (ELG). Compared to ULM and ELG, the sites SOT, BER and BRM have a larger upper tail in their distribution indicating a greater frequency of large nuclear $^{14}CH_4$ emission pulses at these sites.

https://doi.org/10.5194/egusphere-2026-5725
Preprint. Discussion started: 3 November 2026
© Author(s) 2026. CC BY 4.0 License.

The urban site BER has the largest dilutions in $\Delta(^{14}C, CO_2)$ (Fig. 4B), as well as the greatest increases in CO_2 mole fraction, implying it has the largest peak contributions of fossil CO_2 sources, especially in the winter months. Despite their geographic

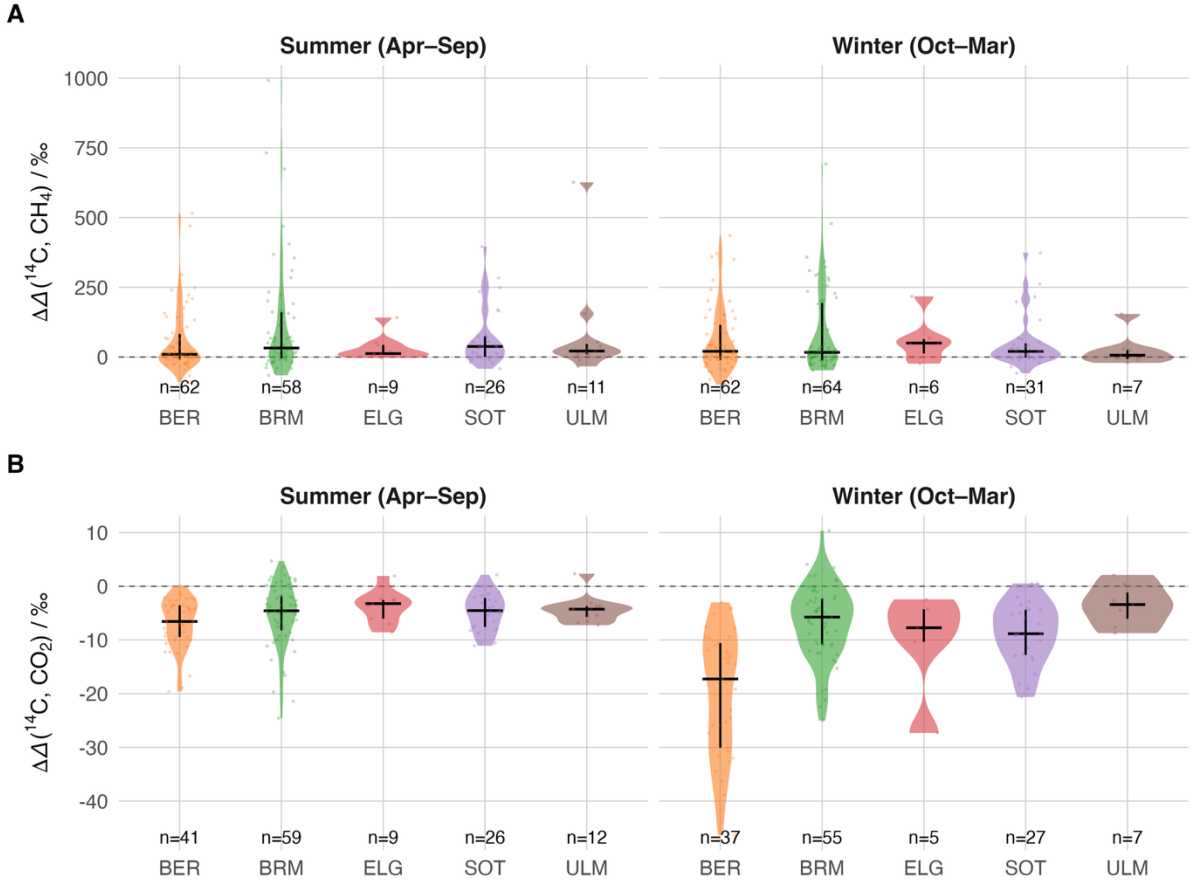


Figure 4: Distribution of measured $\Delta\Delta(^{14}C, CH_4)$ (A) and $\Delta\Delta(^{14}C, CO_2)$ (B), representing the respective $\Delta(^{14}C)$ values of Plateau sites relative to the JFJ background with their distribution shown as violin plots, and separated by season (Summer = April-September, Winter = October-March). Data source is the same as presented in Figs. 2 and 3. Horizontal bars show the median, vertical bars the interquartile range, points individual observations. The dashed line marks zero difference relative to JFJ.

proximity, ULM shows a visibly less depleted and narrower $\Delta\Delta(^{14}C, CO_2)$ distribution than BER; this reflects both ULM's substantially smaller sample size and its higher elevation (937 m a.s.l. vs. BER's 561 m), which likely reduces its exposure to near-surface urban and industrial $^{14}CO_2$ sources relative to BER. Influences of fossil fuel CO_2 sources are also often seen at the other lowland sites. In some isolated cases, positive $\Delta\Delta(^{14}C, CO_2)$ values are visible: this is for example the case at BRM (January 21st, 2021, and January 6th, 2023), ULM (May 16th, 2023), and SOT (June 29th, 2021), which could partly be due to a wind regime bringing a temporarily increased nuclear signal to these sites.

A seasonal breakdown reveals contrasting patterns for $\Delta\Delta(^{14}C, CO_2)$ and $\Delta\Delta(^{14}C, CH_4)$. For $\Delta\Delta(^{14}C, CO_2)$, a clear winter depletion is visible at all sites, most pronounced at the urban site BER (median −17.3 ‰ in winter vs. −6.6 ‰ in summer).

https://doi.org/10.5194/egusphere-2026-5725
Preprint. Discussion started: 3 November 2026
© Author(s) 2026. CC BY 4.0 License.

This is consistent with increased fossil CO_2 emissions from heating and reduced boundary layer mixing during the cold season, made especially evident by the increased tailing towards negative values. Rural sites show a more moderate seasonal contrast (e.g., SOT: −8.8 ‰ vs. −4.5 ‰; BRM: −5.7 ‰ vs. −4.6 ‰). In contrast, $\Delta\Delta(^{14}C, CH_4)$ shows no consistent seasonal pattern across sites: BRM and SOT exhibit higher median values in summer than winter (BRM: +32.1 ‰ vs. +16.6 ‰; SOT: +37.9 ‰ vs. +20.1 ‰), the opposite of what would be expected from a pure fossil CH_4 seasonality.

3.2. Evaluation of simulated $\Delta(^{14}C, CO_2)$ and $\Delta(^{14}C, CH_4)$

The atmospheric transport model allows attributing the signals to different sources and sinks as shown in the next sections. To evaluate how well the model reproduces the actual observations, correlations between measurements (obs) and simulated values (sim), for both $\Delta\Delta(^{14}C, CH_4)$ and $\Delta\Delta(^{14}C, CO_2)$ at all lowland sites are shown in Figs. 5A and 5B. The zoomed-in panels (Figs. 5C and 5D) focus on the moderate-depletion range ($\Delta\Delta > -30$ ‰ on both axes) to give a clearer view of the behaviour across all sites. Site-specific correlation graphs are available in Fig. E1.

For CO_2, the model captures the general behaviour reasonably well on average. A notable exception is BER, where the model systematically predicts larger $\Delta\Delta(^{14}C, CO_2)$ depletions than observed, particularly for the most negative values, consistent with an overestimation of fossil CO_2 accumulation at this urban site. In the zoomed-in view (Fig. 5C), BRM shows the widest range of $\Delta\Delta(^{14}C, CO_2)$ values among rural sites. Its longer record (2019–2023) has had more opportunities to capture episodic local-influence events, and BRM may also be exposed to a wider range of local source influences than the other rural sites. SOT's shorter record (from 2021) has sampled fewer such extremes, contributing to its more compact distribution. Similarly, despite their geographic proximity, BER shows a markedly larger spread toward more depleted $\Delta\Delta(^{14}C, CO_2)$ values than ULM. BER's much larger sample size increases the likelihood of capturing episodic depletion events; ULM's higher elevation (937 m a.s.l. vs. BER's 561 m) may also reduce its exposure to near-surface urban fossil fuel emissions relative to BER, contributing to the remaining difference in distribution.

As for CH_4 (Fig. 5B and 5D), both panels show episodic elevated $\Delta\Delta(^{14}C, CH_4)$ values driven by nuclear contamination events rather than depletions due to fossil sources. These are primarily visible in observations at BRM, BER and SOT, reflecting the influence of NPP Gösgen on these sites. BRM and BER stand out with larger overall spreads due to their longer measurement records.

https://doi.org/10.5194/egusphere-2026-5725
Preprint. Discussion started: 3 November 2026
© Author(s) 2026. CC BY 4.0 License.

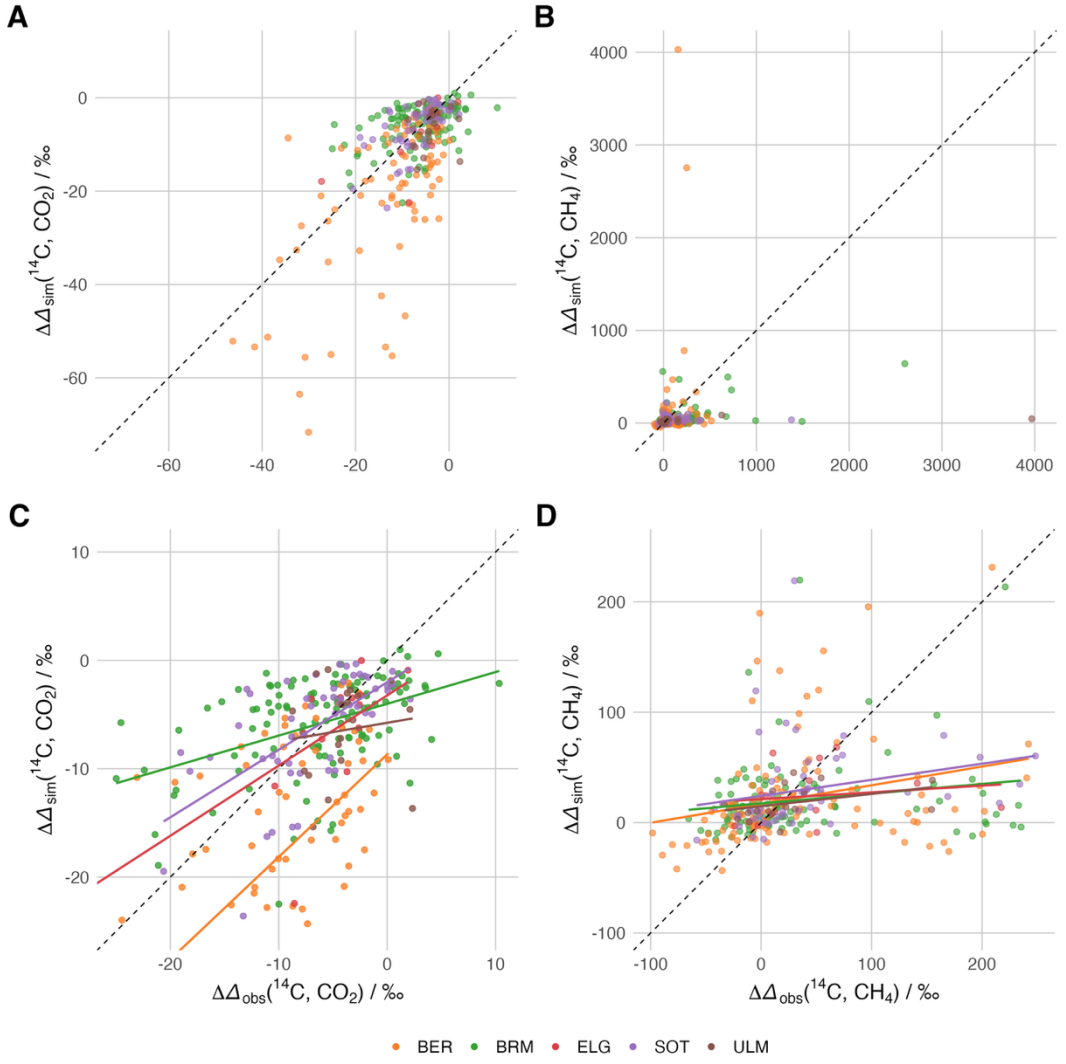


Figure 5: Correlation plots between the in-situ measured (obs) and the simulated (sim) of both $\Delta\Delta(^{14}C, CO_2)$ (A and C) and $\Delta\Delta(^{14}C, CH_4)$ (B and D) for all the Plateau sites. The subplots C and D are zoomed-in versions of A and B (≥ −25 ‰ for CO2, < 250 ‰ for CH_4) and trendlines (based on the full dataset) have been added to highlight per-site relationships. In each subplot, the black dashed line shows the 1:1 relationship.

Temporal $\Delta(^{14}C, CO_2)$ and $\Delta(^{14}C, CH_4)$ comparisons between simulations and measurements for the 2022-2023 period at the three longest-running sites (BER, BRM, and SOT) are shown in Fig. 6. For $\Delta(^{14}C, CO_2)$ (left panels), simulations generally captured the seasonal trends well at all sites, with values ranging from −10 to −60 ‰ at BER, −5 to −25 ‰ at BRM, and −4 to −23 ‰ at SOT. The model reproduced the winter depletion in ^{14}C from fossil emissions as well as the relative summer enrichment. However, notable discrepancies with measurements occurred: at BER, most observations (both in winter and summer) showed a higher $\Delta(^{14}C, CO_2)$ than the simulation, but more intensified in winter where strong simulated depletions were detected. This indicates an overestimation of fossil CO_2 accumulation in the urban area, similarly

https://doi.org/10.5194/egusphere-2026-5725
Preprint. Discussion started: 3 November 2026
© Author(s) 2026. CC BY 4.0 License.

to Figs. 5A and 5C. In contrast, SOT observations showed more depleted Δ(^{14}C, CO_2) values compared to simulations in the winter season. At BRM, observed values matched the simulation relatively well, except for one large winter depletion in early 2022. These patterns are reflected quantitatively in the mean model biases (sim − obs): −6.0 ± 10.8 ‰ at BER (n = 49),

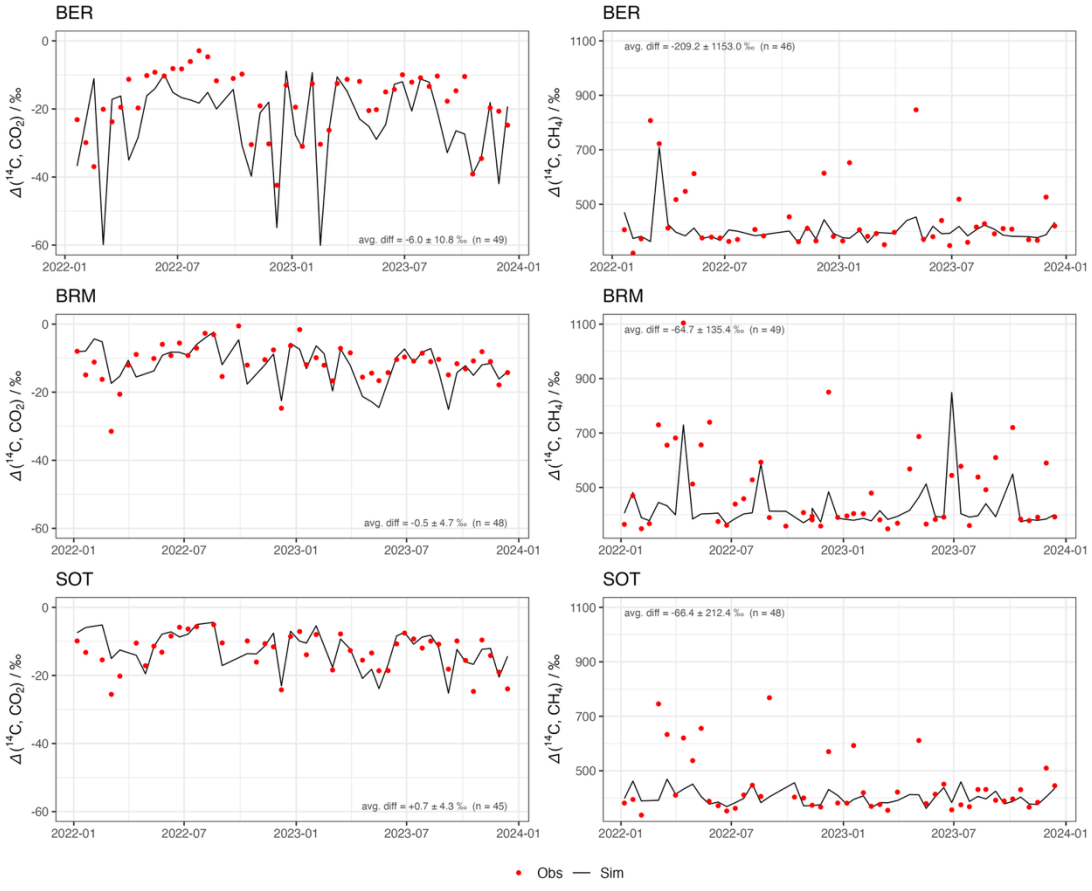


Figure 6: Timeseries of simulated Δ(^{14}C, CO_2) and Δ(^{14}C, CH_4) (Sim, black line) compared to the measurements (Obs, red dots) in 2022-2023 for the 3 sites with the longest measurement periods (BER, BRM, and SOT). For $^{14}CH_4$ measurements, one outlier was removed from the plot (June 14th, 2023), see section 3.1.1.

−0.5 ± 4.7 ‰ at BRM (n = 48), and +0.7 ± 4.3 ‰ at SOT (n = 45), confirming that BRM and SOT are nearly unbiased while BER shows a possible negative offset, although not statistically significant.

For Δ(^{14}C, CH_4) (Fig. 6, right panels), simulations matched the baseline levels (350 – 400 ‰) reasonably well at all sites. However, they failed to reproduce several high amplitude peaks, especially for BER and SOT. Peaks were better reproduced by simulations at BRM, but their amplitude was usually only partly captured, and only once did the simulations overestimate observed Δ(^{14}C, CH_4), in summer 2023. The mean biases (sim − obs) were −65 ± 135 ‰ at BRM, −66 ± 212 ‰ at SOT, and −209 ± 1153 ‰ at BER, with standard deviations an order of magnitude larger than the measurement uncertainty (≈ 11 ‰), reflecting the episodic nuclear $^{14}CH_4$ releases rather than a systematic model offset. These discrepancies reflect the challenge

https://doi.org/10.5194/egusphere-2026-5725
Preprint. Discussion started: 3 November 2026
© Author(s) 2026. CC BY 4.0 License.

of simulating sporadic local and regional nuclear $^{14}CH_4$ releases with low frequency emission data and the problem of accurately transporting point-source emissions to near-by receptors. For Swiss observations, this overwhelming nuclear signal cannot yet be reliably filtered out, and thus fossil vs biogenic $^{14}CH_4$ source apportionment cannot be achieved reliably.

3.3. Nuclear ^{14}C influence

The simulated sources of nuclear influence to $^{14}CH_4$ and $^{14}CO_2$ at the three longest-running sites are shown in Fig. 7. For $^{14}CH_4$ (Fig. 7A), Swiss nuclear facilities dominate the simulated nuclear influence at BER and BRM, with the NPP Gösgen (GSG) being by far the largest contributor, particularly at BER and BRM which are the closest to this PWR. The contribution from NPP Beznau 1-2 (BEZ) is secondary but non-negligible at both sites. At SOT, which is located further west and closer to the French border, the total nuclear signal is lower in magnitude, and the relative contribution of the non-Swiss sources is proportionally larger, with French NPPs contributing more on average than Swiss NPPs. France contributes substantially at all sites (about 18–21 ‰ on average, mostly from individually resolved French NPPs), whereas Germany and the rest of Europe contribute only marginally to the simulated $^{14}CH_4$ influence at all sites. The temporal evolution of the

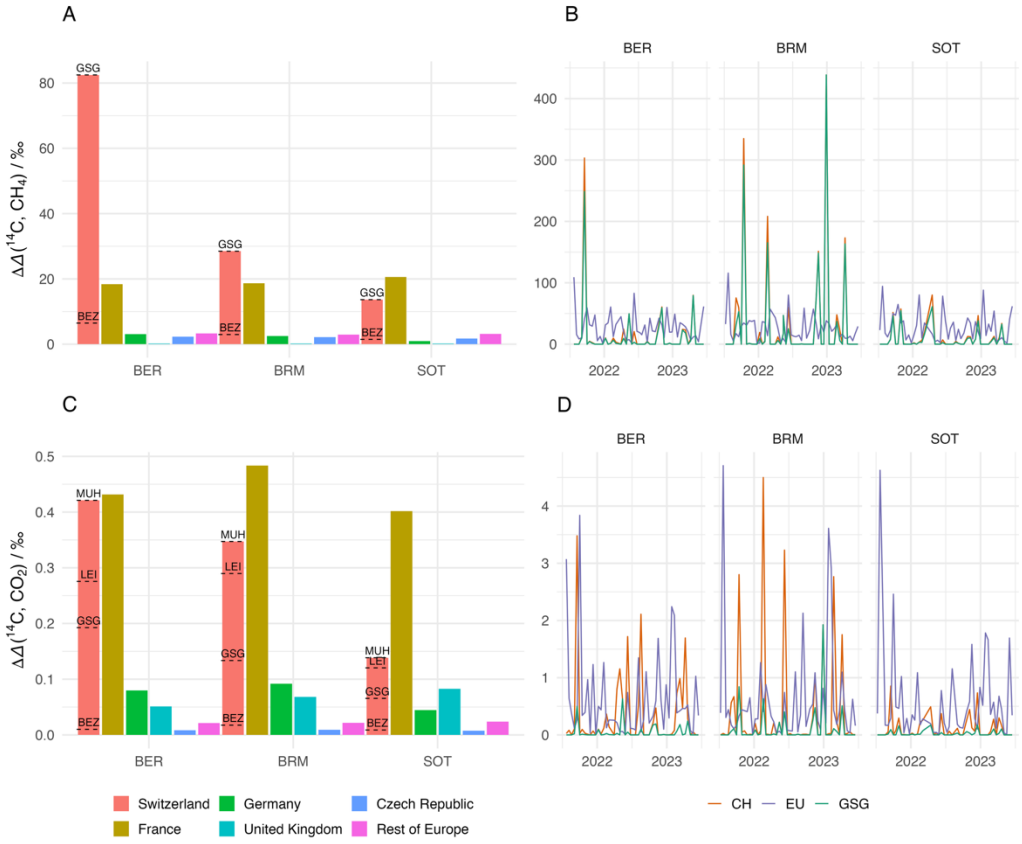


Figure 7: Plots showing the simulated nuclear influence on $^{14}CH_4$ and $^{14}CO_2$ across the 3 main sites (BER, BRM, and SOT). A-C: Barplot showing the mean nuclear origin of ^{14}C for both $^{14}CH_4$ (A) and $^{14}CO_2$ (C) for the entire measurement period (2021-2023 for BER, 2019-2023 for BRM, and 2021-2023 for SOT) divided between Swiss and European reactors (i.e., France, Germany, UK, Czech Republic, and the rest of Europe). LEI and MUH have no $^{14}CH_4$ contribution. B-D: Timeseries of the simulated nuclear influence on $^{14}CH_4$ (B) and $^{14}CO_2$ (D) across 2022 and 2023 for BER, BRM, and SOT, differentiating between Swiss (CH), European (EU), and highlighting GSG specifically.

https://doi.org/10.5194/egusphere-2026-5725
Preprint. Discussion started: 3 November 2026
© Author(s) 2026. CC BY 4.0 License.

nuclear $^{14}CH_4$ influence (Fig. 7B) shows a strongly episodic character at all sites, with sharp peaks of up to 300 ‰ at BER and 400 ‰ at BRM superimposed on a low-level baseline. Despite these larger peak excursions at BRM, BER shows a higher mean nuclear contribution overall (Fig. 7A); GSG dominates both sites, so this reflects a difference in transport coupling rather than in source behavior: BER appears to be more frequently and moderately connected to the Gösgen plume, whereas BRM's connection is rarer but occasionally more concentrated, producing sharper, more isolated excursions against an otherwise lower baseline. Highly episodic influences are simulated even though the highest temporal resolution in NPP emissions is monthly-to-annual, due to episodic atmospheric transport from the nuclear point sources to the observation sites. The nuclear influences are predominantly driven by Swiss NPPs (CH, orange line), GSG in particular (green line), with occasional contributions from other EU sources.

For $^{14}CO_2$ (Fig. 7C-D), the overall nuclear influence is approximately two orders of magnitude smaller than for $^{14}CH_4$, with mean contributions of about 0.7–1.0 ‰. French sources, dominated by the La Hague NFRP, contribute as much as or more than the Swiss NPPs at all three sites (about 0.4–0.5 ‰ on average). At BER and BRM, the Swiss NPPs, notably MUH (despite its closure in 2019), and Leibstadt (LEI) are the main contributors among Swiss sources, while UK influences are proportionally more significant at SOT, mainly due to the Sellafield NFRP (until 2022). The simulations indicate more frequent episodes of strong nuclear influences on $\Delta(^{14}C, CO_2)$ than $\Delta(^{14}C, CH_4)$, with episodic peaks up to about 3.5–4.7 ‰ at BER and BRM and 4.6 ‰ at SOT, where non-Swiss sources dominate (Fig. 7D).

3.4. Source apportionment of CO_2 and CH_4 over Switzerland

Fossil CO_2 contributions derived from raw ^{14}C mass balance, nuclear-corrected ^{14}C mass balance (see Turnbull et al., 2006; Appendix F, Fig. F1), and atmospheric transport simulations are compared for the three main sites in Fig. 8. “Raw ^{14}C” (red) denotes the fossil CO_2 estimate obtained by applying the mass balance approach directly to the observed $\Delta(^{14}C, CO_2)$, treating all depletion relative to background as fossil-derived. "Corrected ^{14}C" (green) instead first subtracts the simulated nuclear $\Delta\Delta(^{14}C, CO_2)$ contribution (Section 2.4.5) from the observed value before applying the same mass balance, isolating the fossil-derived component from nuclear contamination. The difference between the two curves at a given site and time therefore reflects the magnitude of the simulated nuclear correction. At all three sites, the simulated fossil CO_2 (dashed blue) shows the larger variability and generally the higher fossil CO_2, particularly during winter months (shaded grey), compared to the $\Delta(^{14}C, CO_2)$-observation derived estimate. The raw and corrected ^{14}C-derived estimates track each other closely at most sites and times, suggesting that the nuclear $^{14}CO_2$ correction has a limited effect on the final fossil CO_2 estimate. This is consistent with the small magnitude of the nuclear $^{14}CO_2$ signal relative to the fossil CO_2 signal discussed in Section 3.3.

BER consistently shows the highest fossil CO_2 among the three sites, with raw and corrected estimates reaching up to 15-20 µmol mol^{-1}, reflecting its urban setting. There, ^{14}C-derived estimates tend to be higher in the simulations than the observed values, particularly during winter peaks, which is consistent with the overestimation of winter CO_2 mole fraction peaks discussed in Section 3.2. At BRM and SOT, fossil CO_2 contributions are more moderate and generally below 10 µmol mol^{-1}.

https://doi.org/10.5194/egusphere-2026-5725
Preprint. Discussion started: 3 November 2026
© Author(s) 2026. CC BY 4.0 License.



Figure 8: Timeseries of fossil CO_2 contributions for the 3 main sites (BER, BRM, and SOT) across the 2021-2023 period. Fossil contributions are calculated from three approaches: raw ^{14}C-based mass balance (Raw ^{14}C, red), nuclear-corrected ^{14}C-based mass balance (Corrected ^{14}C, green), atmospheric transport simulation ^{14}C-based mass balance (Simulated, dashed blue). Winter periods (01.10– 01.04) are highlighted in light grey.

^{14}C-derived fossil fuel contributions at BER are systematically lower than the simulation (corrected − simulated: −3.4 ± 5.5 µmol mol−1; Fig. F1), indicating that the model overestimates fossil CO_2 accumulation at this urban site. This offset is larger in winter (−4.2 ± 7.4 µmol mol^{-1}) than in summer (−2.8 ± 2.8 µmol mol^{-1}), consistent with a model bias that is amplified under shallow boundary layer conditions. At BRM and SOT, the offset is near-zero in both seasons, meaning that the model is representative of influences at rural sites.

https://doi.org/10.5194/egusphere-2026-5725
Preprint. Discussion started: 3 November 2026
© Author(s) 2026. CC BY 4.0 License.

An equivalent source apportionment was attempted for CH_4; however, the nuclear correction led to a severe overcorrection of the fossil CH_4 signal, yielding physically implausible results. This is a direct consequence of the unresolved nuclear $^{14}CH_4$ signal discussed in Section 3.3, where episodic releases are insufficiently captured by the available emission data. These results are presented in Fig. F2 for completeness.

4. Discussion

4.1. Multi-site monitoring network design

The tall tower network established across the Swiss Plateau provides complementary spatial coverage to existing European ^{14}C monitoring efforts. Our multi-site approach captures regional gradients in both $^{14}CO_2$ and $^{14}CH_4$ across an area with heterogeneous emission sources, building on the single, background Swiss ICOS $^{14}CO_2$ measurements at JFJ (Emmenegger et al., 2025; Levin et al., 2022). This design is conceptually similar to regional networks deployed in other urbanized regions (Graven et al., 2018; Turnbull et al., 2019), and, to our knowledge, is the first multi-year network in Switzerland integrating radiocarbon in both CO_2 and CH_4, complementing earlier $^{14}CH_4$ studies in other nuclear-influenced regions (Eisma et al., 1994, 1995; Zazzeri et al., 2023).

The sampling strategy evolved significantly over the study period. Initially, morning grab samples were taken, which resulted in larger scatter due to nocturnal accumulation of emissions. Shifting to afternoon sampling (14:00-15:00 UTC) in November 2022 improved comparability across sites and reduced the mean winter model-observation bias at BER from +13.7 ± 19.2 ‰ to +3.8 ± 10.7 ‰ in winter (Fig. E2). At JFJ, the April 2023 transition to integrated nighttime sampling via JASS reduced variability in both $^{14}CH_4$ and ancillary parameters (Rn, CH_4 mole fraction; see Section 2.4.3), yielding values closer to monthly means and better representing free tropospheric conditions (Conen and Zimmermann, 2020). This methodological refinement demonstrates the value of integrated sampling for background site characterization, consistent with findings from other high-altitude stations (Laemmel et al., 2026).

A word of caution is warranted regarding the representativeness of the BER site. The model's systematic overestimation of fossil CO_2 at BER is larger than is typical and likely reflects a genuine limitation of the transport model's 1 km × 1 km horizontal grid, which cannot resolve building-scale urban canopy effects. BER's sampling inlet is a lab window in central Bern, situated within a street canyon; a single 1 km grid cell at this location necessarily contains a mix of heavily trafficked streets, heating infrastructure, and quieter courtyards, and the model assigns one spatially-averaged mole fraction to the entire cell regardless of where within it the true emission density is concentrated. If the inlet's actual local exposure differs systematically from that grid-cell average; for instance, if it is comparatively sheltered from the nearest major street relative to the cell as a whole, this alone could produce a persistent model-observation offset unrelated to any error in the underlying emission inventory.

https://doi.org/10.5194/egusphere-2026-5725
Preprint. Discussion started: 3 November 2026
© Author(s) 2026. CC BY 4.0 License.

4.2. Biospheric CO_2 fluxes and $^{14}CO_2$ attribution

The updated heterotrophic respiration ^{14}C signature (−5.3 ± 1.6 ‰ vs. previous +80 ‰), a flux-weighted estimate based on land-use specific measurements (Minich et al., 2026) represents a major refinement in our understanding of ecosystem ^{14}C fluxes over Switzerland. Unlike this highly-enriched +80 ‰ value, which implied respiration was dominated by old, slowly-cycling carbon fixed near the atmospheric bomb-peak, the new near-background signature implies a larger contribution of newly assimilated carbon and possibly a non-negligible contribution from older sources (pre-bomb peak) from peatland, p.ex. It also means that respiration now acts to stabilize rather than enrich atmospheric $\Delta(^{14}C, CO_2)$, altering the interpretation of rural site measurements. The good agreement between simulated and observed $\Delta(^{14}C, CO_2)$ at sites like BRM and SOT, despite their strong respiration influence, supports this revised signature. However, the Minich et al. (2026) dataset is spatially and temporally limited, and seasonal or land-use-specific variations in respiration ^{14}C remain poorly constrained, a critical uncertainty for atmospheric modelling (Wenger et al., 2019).

We also tested an empirical correction to the simulated respiration flux magnitude (Section 2.4.4), fit to BRM's afternoon CO_2 data; this improved the CO_2 mole fraction fit at BRM itself but did not measurably improve simulated-observed $\Delta(^{14}C, CO_2)$ agreement at any site, and did not consistently transfer to other Plateau sites. Summer CO_2 mole fraction underestimation (Fig. D1; Table D1) may indicate limitations in VPRM's representation of agricultural phenology and water stress, as noted in similar studies (Gourdji et al., 2022). Future implementations incorporating harvest timing, crop-specific enhanced vegetation index (EVI) adjustments, and soil moisture constraints into VPRM may help address this flux-magnitude uncertainty, though this remains to be tested. Together, these results suggest the respiration ^{14}C signature is now reasonably well constrained, and that residual model-observation mismatch at rural sites more likely reflects uncertainty in the magnitude and timing of the simulated respiration flux itself, rather than its isotopic composition.

Comparing ^{14}C-derived and simulated (inventory-based) fossil CO_2 estimates provides a direct test of the reported Swiss emission inventories. At BRM, the two approaches agree closely on average (2.4 ± 2.8 vs. 2.8 ± 2.1 µmol mol^{-1}, 2021–2023), supporting the reliability of the underlying inventory at this well-characterised rural site. At BER, the ^{14}C-derived estimate is somewhat lower than the simulation on average (6.1 ± 4.9 vs. 9.6 ± 7.4 µmol mol^{-1}), though the spread at both sites is large relative to this offset, and we do not interpret it as a robust indication that urban fossil emissions are over-reported. These results are robust to the background definition: alternative backgrounds change the mean fossil CO_2 estimates by at most 0.64 µmol mol^{-1} and do not change the sign of the offsets (Appendix C, Table C1). Site-to-site differences in offset sign are not of consistent direction (Fig. 8; Table F1), arguing against a shared meteorological cause such as PBL height misrepresentation, and instead point to site-specific factors, potentially including the limited ability of a 1 km × 1 km transport model to resolve urban-canopy effects at BER (Section 4.1). This comparison illustrates the kind of independent, top-down check that ^{14}C monitoring can provide on bottom-up emission reporting, complementary to the network's role in establishing baseline atmospheric levels (Kretschmer et al., 2012; Pieber et al., 2022).

https://doi.org/10.5194/egusphere-2026-5725
Preprint. Discussion started: 3 November 2026
© Author(s) 2026. CC BY 4.0 License.

4.3. Nuclear $^{14}CH_4$ and implications for source apportionment

Atmospheric $^{14}CH_4$ measurements reveal that nuclear emissions from PWRs in Switzerland and neighboring countries significantly influence the atmospheric signature across all sites, including JFJ, which is considered a European background station (Laemmel et al., 2026). At JFJ, the mean nuclear contribution was +7 ± 9 ‰, with individual samples reaching up to this 58 ‰, demonstrating that even remote high-altitude sites are not immune to regional nuclear contamination. At lowland sites on the Swiss Plateau, the influence is even more pronounced, with frequent excursions above background and such exceptional peaks as > 4000 ‰ observed on April 19, 2023, at BER and ULM.

Historically, simulations of nuclear ^{14}C influence relied on emission factors that converted annual electricity production into annual ^{14}C release estimates (Eisma et al., 1995; Wenger et al., 2019; Zazzeri et al., 2018). While this approach may be adequate for BWRs, which release $^{14}CO_2$ in a relatively continuous manner, it fundamentally misrepresents PWR behavior. PWR ^{14}C emissions (predominantly as $^{14}CH_4$) are sporadic and often concentrated during outage or maintenance periods (Espic et al., 2025; Kunz, 1985; Stenström et al., 1995). If identified, these events could be filtered out for future sampling strategies. The updated inventory used in this study, with monthly data for Swiss NPPs and quarterly data for France and Germany, represents an improvement over annual averages but remains insufficient to resolve hourly to daily release events. The April 19, 2023, event illustrates this challenge directly: exceptionally high $\Delta(^{14}C, CH_4)$ values were measured at BER (8266 ‰), ULM (4345 ‰), and to a lesser extent at SOT (2963 ‰). Elevated noble gas emissions were reported at NPP Gösgen beginning the previous evening, and easterly winds on that day are consistent with transport from Gösgen (ca. 60 km away) to these sites. Similar short-duration release events have been documented at Gösgen during its 2019 annual revision period, where a single event lasting only a few hours accounted for ≈ 8 % of the plant's total annual $^{14}CH_4$ emissions (Espic et al., 2025). Such large temporal variability leads to systematic underprediction of peak mole fractions and overprediction during quiescent periods, limiting the utility of model-based nuclear corrections.

This contamination severely compromises $^{14}CH_4$-based fossil source apportionment. When unresolved nuclear enrichment occurs, the residual ^{14}C excess is misattributed to biogenic CH_4, driving inferred fossil fractions to negative values. Similar challenges have been documented in the Netherlands (Eisma et al., 1994, 1995) and the UK (Zazzeri et al., 2023), but the sporadic PWR release pattern exacerbates the problem in nuclear-dense regions like Switzerland. In contrast, $^{14}CO_2$-based fossil CO_2 attribution remains viable despite nuclear contamination. The nuclear $^{14}CO_2$ signal is almost two orders of magnitude smaller (+0.2 ± 0.4 ‰ vs. +7 ± 9 ‰ for $^{14}CH_4$; (Laemmel et al., 2026), and BWR/NFRP emissions are temporally more stable than PWR releases, making them easier to simulate with monthly resolution.

Future progress in $^{14}CH_4$ source apportionment shall require high-frequency nuclear emission constraints. One promising avenue is the use of noble gas stack monitors as proxies for ^{14}C releases (Espic et al., 2025). For Switzerland, where such monitoring is already in place, correlations between noble gas activity and $^{14}CH_4$ releases could enable reconstruction of hourly emission profiles from archived stack data. Additionally, emerging technologies such as cavity ring-down spectroscopy (CRDS) offer the potential for in-situ, real-time ^{14}C monitoring at nuclear facilities (Genoud et al., 2019;

https://doi.org/10.5194/egusphere-2026-5725
Preprint. Discussion started: 3 November 2026
© Author(s) 2026. CC BY 4.0 License.

Lehmuskoski et al., 2021), which may provide continuous high-frequency emission data rather than relying on retrospective proxies. Without such improvements, $^{14}CH_4$ will remain unreliable for quantitative fossil CH_4 attribution in PWR-influenced regions, and alternative tracers such as ^{13}C (Basu et al., 2022; Fujita et al., 2025) and clumped isotopes (Haghnegahdar et al., 2023) will be necessary for robust source apportionment. While nuclear $^{14}CO_2$ contamination is currently much smaller than for $^{14}CH_4$ (+0.2 ± 0.4 ‰ on average), it relies on the same coarse, monthly/quarterly-resolved emission inventories; improved temporal resolution of nuclear ^{14}C release data would further reduce residual uncertainty in the nuclear-corrected fossil CO_2 estimates (Fig. 8).

4.4. Practical recommendations and future directions

Key practical steps for improving the application of ^{14}C observation-based constraints on CH_4 and CO_2 emissions in Switzerland include:

1. **Improved nuclear emission inventories**: Collaboration with NPP operators to access higher-frequency (daily to hourly) ^{14}C release data, or development of noble gas-based ^{14}C emission proxies, would substantially improve simulation accuracy. A recently published compilation of global nuclear ^{14}C emissions ((Laemmel et al., 2025); 10.5281/zenodo.15034662) provides a comprehensive baseline for atmospheric modelling and should be maintained and updated as new emission data become available.

2. **Enhanced biospheric flux models**: Integration of crop-specific phenology, harvest timing, and soil moisture stress into VPRM (or transition to more advanced models like VPRM-SMAP; Gourdji et al., 2022) would reduce summer biases and improve $^{14}CO_2$ attribution.

3. **Complementary tracer constraints**: $\delta(^{13}C)$ measurements on CO_2 and CH_4 can provide independent source information, as well as combines O_2 measurements, to help distinguish different oxidation sources. For CH_4, clumped isotope measurements ($\Delta^{13}CH_3D$) may help distinguish thermogenic from microbial sources without nuclear interference.

4. **Vertical profiling of trace gases**: Occasional unmanned aircraft or tethered balloon profiles would help diagnose vertical mixing biases and improve understanding of convective mixing over complex terrain.

5. **Higher-frequency, integrated sampling at lowland sites**: Model-observation mismatch in ^{14}C-based inverse modelling is often dominated by random error, so daily sampling could substantially improve source attribution; achieving this in practice likely requires integrated rather than discrete grab sampling, as demonstrated for JFJ (Section 3.1.1). However, at boundary-layer sites, integration would reduce the temporal resolution needed to resolve sources by wind direction, unlike at a background site.

https://doi.org/10.5194/egusphere-2026-5725
Preprint. Discussion started: 3 November 2026
© Author(s) 2026. CC BY 4.0 License.

6. **Development of an inversion framework**: Rather than relying solely on forward transport simulations to interpret atmospheric ^{14}C observations, a formal inversion framework could jointly optimize fossil and biospheric flux estimates while using the ^{14}C data itself to help constrain simulated nuclear influences, rather than treating them as an independent, one-way correction. This would provide a more rigorous, quantitative link between the atmospheric observations presented here and emission inventory verification.

Together with the recommendations above, an inversion framework built on this multi-site ^{14}C network (point 6) could provide genuine, quantitative top-down constraints on Swiss and regional fossil CO_2 emissions, rather than relying solely on the forward mass-balance approach used here. For $^{14}CH_4$, given that nuclear contamination precludes robust fossil source apportionment in this and similarly nuclear-influenced regions, we suggest its primary value going forward lies not in fossil CH_4 apportionment but in constraining nuclear ^{14}C emissions themselves within such an inversion framework, repurposing the same nuclear signal that currently limits its use as a diagnostic of NPP behavior instead. As nuclear power expands globally, this redefined role for $^{14}CH_4$ monitoring may become increasingly relevant in other nuclear-influenced regions.

5. Conclusion

This study presents, to our knowledge, the first multi-year, multi-site monitoring network for simultaneous atmospheric $^{14}CO_2$ and $^{14}CH_4$ measurements in Switzerland, with new observations at five sites across the Swiss Plateau for the period 2019-2023, interpreted against the observations at the high-altitude background station Jungfraujoch from the same campaign (Laemmel et al., 2026). Integration with FLEXPART-COSMO atmospheric transport modelling and updated emission inventories has enabled assessment of both fossil fuel emissions and nuclear contamination influences on atmospheric ^{14}C signatures.

For $^{14}CO_2$, the network demonstrates robust performance for fossil CO_2 source apportionment. The updated respiration ^{14}C signature (−5.3 ‰ vs. previous +80 ‰; based on Minich et al., 2026) substantially improved model-measurement agreement at rural sites, while nuclear $^{14}CO_2$ contamination remains negligible (+0.2 ± 0.4 ‰). Fossil CO_2 estimates show expected spatial patterns, with highest values at the urban site BER and good agreement between ^{14}C-derived and inventory-based estimates across seasons. Comparison against inventory-based simulations provides a direct, independent test of reported Swiss emission inventories: at the well-characterised rural site BRM, ^{14}C-derived and simulated fossil CO_2 estimates agree closely, supporting the underlying inventory, while BER shows a modest negative offset that may reflect the limited ability of a about 1 km × 1 km transport model to resolve urban-canopy effects rather than an error in reported emissions. More broadly, the spatial (urban vs. rural) and seasonal (winter-enhanced) patterns in ^{14}C-derived fossil CO_2 closely track Switzerland's reported emission sectors (transport and heating), and the close agreement with inventory-based simulations at the rural sites provides independent corroboration that reported Swiss fossil CO_2 emissions are not substantially under- or over-estimated at the regional scale.

https://doi.org/10.5194/egusphere-2026-5725
Preprint. Discussion started: 3 November 2026
© Author(s) 2026. CC BY 4.0 License.

In contrast, $^{14}CH_4$ measurements reveal pervasive nuclear contamination that severely limits fossil CH_4 source apportionment. Sporadic PWR releases cannot be adequately resolved with monthly/quarterly emission inventories, leading to systematic over- or under-correction and physically implausible negative fossil CH_4 estimates. This demonstrates a fundamental limitation of $^{14}CH_4$ for quantitative source attribution in nuclear-dense regions without substantial improvements in emission temporal resolution or in situ monitoring capabilities.

Continued operation of this network, combined with methodological refinements (higher-frequency nuclear emission data, improved biospheric flux models, complementary isotopic tracers), may provide critical long-term constraints on Swiss and regional European fossil emissions. The contrasting success of $^{14}CO_2$ versus $^{14}CH_4$ underscores the need for tracer-specific strategies and highlights the growing challenge of nuclear contamination as nuclear power expands globally.

https://doi.org/10.5194/egusphere-2026-5725
Preprint. Discussion started: 3 November 2026
© Author(s) 2026. CC BY 4.0 License.

Appendix A: Sites, sampling and inter-laboratory comparison

Table A1: Sites information and description

Site	Name	Latitude	Longitude	Elevation (m a.s.l.)	Inlet Height (m a.g.l.)	Site Type	Sampling start date	Description
JFJ	Jungfraujoch	46.54755	7.98534	3454 (station) / 3570 (sphinx)	-	Background	12.2018	High-elevation research station
BER	Bern	46.95295	7.42932	561	10	Urban	10.2018	Lab window
BRM	Beromünster	47.18957	8.17542	798	212.5	Rural	07.2018	Telecommunication tower
SOT	Sottens	46.65593	6.73638	776	46	Rural	06.2021	Telecommunication tower
ULM	Ulmizberg	46.90051	7.43394	937	92	Rural	03.2023	Telecommunication tower
ELG	Elgg-Schneitberg	47.50621	8.86831	674	54	Rural	05.2023	Telecommunication tower

https://doi.org/10.5194/egusphere-2026-5725
Preprint. Discussion started: 3 November 2026
© Author(s) 2026. CC BY 4.0 License.

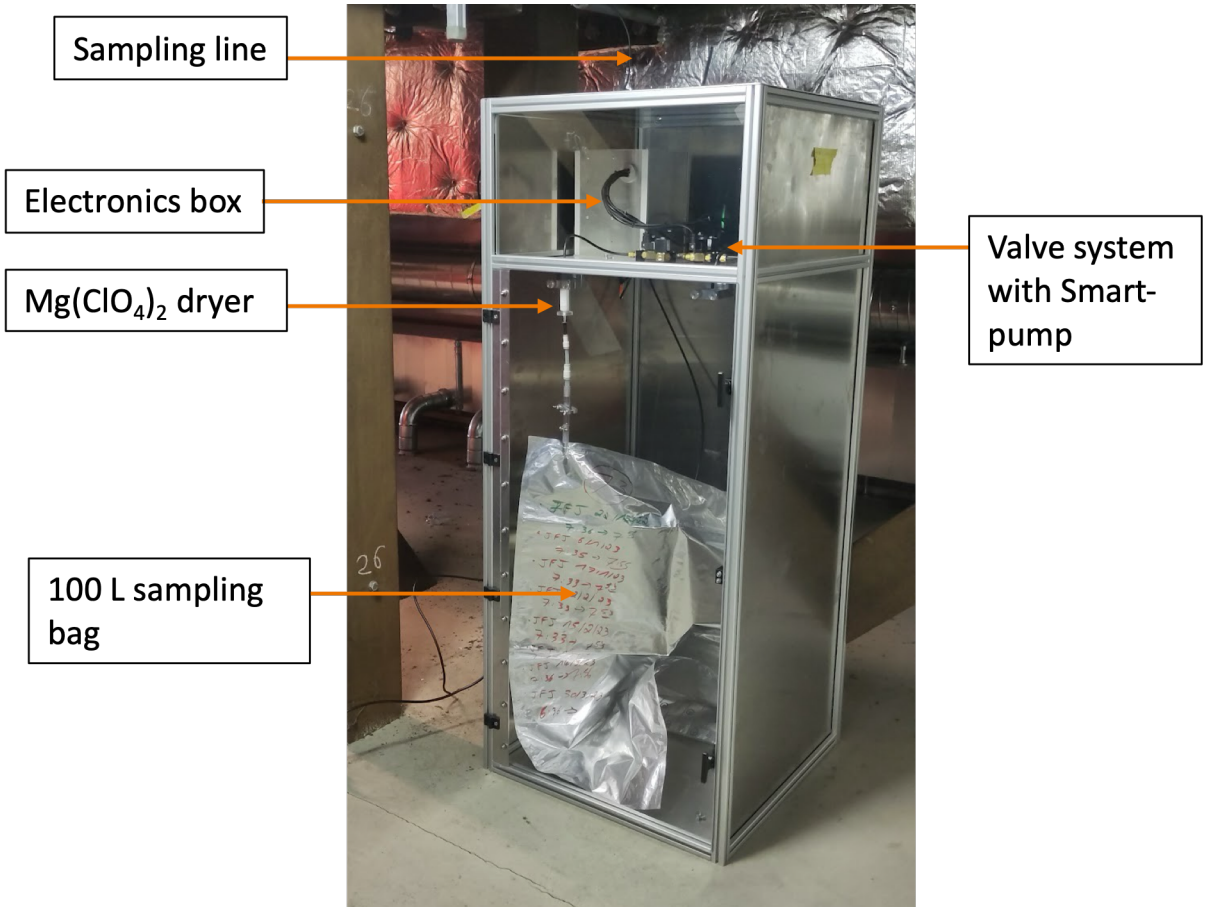


Figure A1: Picture showing the Monitoring Air Sampling System (MASS) installed at ULM, allowing a preprogrammed sampling of air (time and flow). The top part of the metal enclosure contains the electronics controls and the valve system, and the bottom part serves as the housing of the sampling bag.

https://doi.org/10.5194/egusphere-2026-5725
Preprint. Discussion started: 3 November 2026
© Author(s) 2026. CC BY 4.0 License.

In the scope of this paper, ^{14}C measurements were performed at two different laboratories, LARA and LIP, using similar but nevertheless distinct methods. To ensure that results from both laboratories could be combined without bias, we performed regular intercomparison measurements using a pressurized air bottle (PAB) standard throughout 2022 and 2023.

Across both years, the mean PAB $\Delta(^{14}C)$ values for LARA and LIP were −47.1 ± 1.5 ‰ (n = 24) and −47.9 ± 1.7 ‰ (n = 24), respectively, differing by 0.8 ‰. The uncertainty of the mean (σ/√n) was 0.3 ‰ for LARA and 0.3 ‰ for LIP. Breaking down by year, LARA measured −47.0 ± 1.6 ‰ (σ/√n = 0.5 ‰, n = 11) in 2022 and −47.4 ± 1.4 ‰ (σ/√n = 0.4 ‰, n = 13) in 2023, while LIP measured −48.2 ± 1.7 ‰ (σ/√n = 0.5 ‰, n = 11) in 2022 and −47.6 ± 1.7 ‰ (σ/√n = 0.5 ‰, n = 13) in 2023. While LIP values were systematically ≈ 1 ‰ lower than LARA in 2022, this offset decreased to 0.2 ‰ by 2023, suggesting minor procedural differences that were resolved during the study period. The year-to-year differences within each laboratory (0.4 ‰ for LARA, 0.6 ‰ for LIP) were comparable to the inter-laboratory offset. Notably, measurements from 2023 onward showed reduced dispersion, with LARA's standard deviation improving from 1.6 ‰ to 1.4 ‰. Given that these differences are smaller than the atmospheric ^{14}C signals being measured (typically >10 ‰), no correction factors were applied, and measurements from LARA and LIP were merged directly.

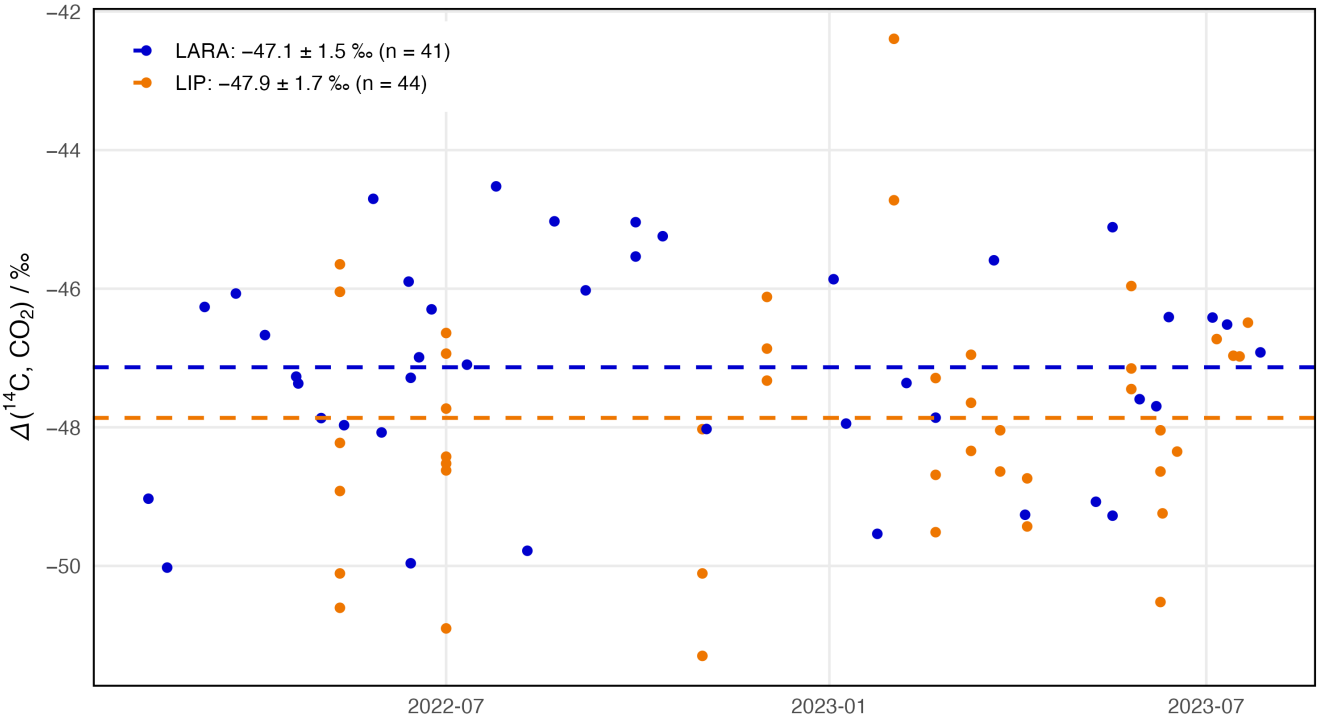


Figure A2: Comparison of the $\Delta(^{14}C, CO_2)$ values of the PAB control air measured at LARA (blue) and LIP (orange) in 2022 and 2023. Dashed lines show the mean values of each laboratory, which are given in the legend with their standard deviations and numbers of measurements.

https://doi.org/10.5194/egusphere-2026-5725
Preprint. Discussion started: 3 November 2026
© Author(s) 2026. CC BY 4.0 License.

Appendix B: Emission sectors and ^{14}C signatures

Table B1: Emission Sector Definitions and ^{14}C Signatures

Sector	$^{14}CO_2$ signature (‰)	$^{14}CH_4$ signature (‰)	Description	Sources
Respiration	−5.3	-	Flux-weighted average across Swiss land-use classes (area fraction × respiration rate), combining measured land-use-specific soil respiration ^{14}C with Swiss land-cover statistics and forest conifer/deciduous composition	Minich et al. (2026); FSO, (2026); NFI, (2026) (see Tables B2 and B3)
GPP	0	-	Photosynthetic CO_2 uptake removes ambient-composition air; to first order this does not alter the $\Delta(^{14}C, CO_2)$ of the remaining air, so no net signature is assigned	This study
Agriculture	-	−9	Low-land grassland soil-respiration ^{14}C signature, used as a proxy for the ^{14}C content of recently-assimilated forage carbon cycled through enteric fermentation and manure management (Swiss livestock agriculture is concentrated on lowland grassland/cropland)	Minich et al., (2026)
Transport	−950	−950	6 % biodiesel content in 2022, total use 44 % benzin, 56 % Diesel for road transport	CARBURA, (2023)
Fossil	−1000	−1000	Pure fossil sources (aviation, solvents, industry emissions)	Emissionenkadaster INFRAS (Heldstab et al., 2021)
Heating	−940	−940	6 % biogas content in gas network for residential heating	Gazenergie-Verband der Schweiz, (2023)
Wood burning	15	15	Modern average signature of wood	Geissbühler et al., (2025); Mohn et al., (2012)
Cement	−850	−850	Based on previous own work, measurement of total ^{14}C content in cement production in CH	Geissbühler et al., (2025)
Waste	−500	-	Based on measurements at waste incineration plants for CO_2 / no separate CH4 waste flux is tracked in the simulation	Mohn et al., (2012)

https://doi.org/10.5194/egusphere-2026-5725
Preprint. Discussion started: 3 November 2026
© Author(s) 2026. CC BY 4.0 License.

Table B2: Measured $\Delta(^{14}C, CO_2)$ signatures of soil-respired CO_2 at Swiss sites across different land-use types, from Minich et al. (2026). $F^{14}C$: fraction modern; $\Delta(^{14}C)$: radiocarbon signature in ‰ relative to the oxalic acid II standard (Stuiver and Polach, 1977). Values are used to derive land-use-specific ^{14}C respiration signatures applied in the atmospheric simulations (see Table B3)

Site	Land use	Sample type	$F^{14}C$	$\Delta(^{14}C)$ / ‰
Lindergut original	peatland original	soil respiration	0.892	−115.81
Underi Site original	peatland original	soil respiration	0.918	−89.53
Rimmerzmatte original	peatland original	soil respiration	0.820	−186.79
Changins no maize	cropland	soil respiration	0.997	−11.70
Changins maize	cropland	soil respiration	1.002	−6.21
Altwi	cropland	soil respiration	0.994	−14.14
Reckenholz	cropland	soil respiration	0.962	−45.62
Chamau	low-land grassland	soil respiration	0.993	−15.17
Jaun	low-land grassland	soil respiration	1.003	−4.94
Muldain	low-land grassland	soil respiration	1.001	−7.24
Schwarzhorn3100	alpine paleo-soil	soil respiration	0.994	−14.13
Schwarzhorn2660	alpine grassland	soil respiration	1.008	−0.01
Schwarzhorn2320	alpine grassland	soil respiration	1.004	−4.21
Bueelenhorn2340	alpine grassland	soil respiration	1.002	−6.72
Radoent2340	alpine grassland	soil respiration	1.009	0.45
Beatenberg	forest	soil respiration	1.018	9.20
Hoelstein control	forest	soil respiration	1.015	6.32
Pfynwald control	forest	soil respiration	1.015	5.75

Table B3: Swiss land-use surface areas, summer and winter soil respiration rates, and mean $\Delta(^{14}C)$ respiration signatures (Minich et al., 2026) used to compute the flux-weighted national respiration signature of −5.3 ± 1.64 ‰ applied in the FLEXPART-COSMO simulations. Land-use surface areas and percentage cover are from the Swiss Federal Statistical Office (FSO, 2026); forest area is split into evergreen (conifer, 62 %) and deciduous/mixed (38 %) sub-classes following the Swiss National Forest Inventory. Low-land and alpine grassland share the same respiration rate, as Minich et al. (2026) report a single combined grassland rate for the two land-use types. The $\Delta(^{14}C)$ value for each land-use category is the mean of measurements within that category from Table B2 (Minich et al., 2026). Each class is weighted by both its areal extent and its annual respiration flux (6 × summer + 6 × winter rate); the resulting flux-weight fraction (∑ = 100 %) gives the flux-weighted mean applied in the atmospheric simulations. The area-weighted mean (weighting by area fraction alone) is shown for reference to illustrate the effect of flux-weighting.

Land Use	Area (km^2)	Area fraction	Summer resp. ($mg\ C\ m^{-2}\ h^{-1}$)	Winter resp. ($mg\ C\ m^{-2}\ h^{-1}$)	Flux-weight fraction (%)	$\Delta(^{14}C, CO_2)$

https://doi.org/10.5194/egusphere-2026-5725
Preprint. Discussion started: 3 November 2026
© Author(s) 2026. CC BY 4.0 License.

		(%)				(‰)
Evergreen forest (conifer)	8147	29.7	82.4	52.2	13.5	9.2
Deciduous + mixed forest	4994	18.2	212.5	108.6	19.7	6.3
Low-land grassland	5186	18.9	221.3	191	26.3	−9.1
Alpine grassland	5024	18.3	221.3	191	25.5	−2.6
Cropland	3811	13.9	193.1	93.2	13.4	−19.4
Peatland	280	1	362.5	114.3	1.6	−130.7
Area-weighted mean (Σ area fraction × Δ(^{14}C))						−2.4
Flux-weighted mean (Σ flux-weight fraction × Δ(^{14}C)) - applied in simulations						−5.3 ±1.6

Appendix C: Background sensitivity

Because JFJ is itself influenced by nuclear emissions and its sampling protocol changed in April 2023 (two-week integrated night-time sampling with JASS), we tested the sensitivity of the fossil CO_2 estimates at BER, BRM and SOT (2021–2023) to six alternative background definitions (Table C1): a nuclear-corrected ICOS background (simulated nuclear $\Delta\Delta(^{14}C, CO_2)$ at JFJ: 0.31 ± 0.22 ‰), our own fortnightly JFJ samples with and without nuclear correction, and ICOS backgrounds averaged over three months or one year or smoothed by a trend-plus-harmonic fit. The mean nuclear-corrected fossil CO_2 changed by at most −0.64 µmol mol^{-1} (SOT, own nuclear-corrected JFJ samples) and by ≤ 0.12 µmol mol^{-1} for all ICOS-based variants; per-sample changes were 0.1–1.2 µmol mol^{-1} (1σ). The corrected − simulated offsets remained between −3.3 and −3.8 µmol mol^{-1} at BER and within ±0.8 µmol mol^{-1} at BRM and SOT, and the sign of the winter offsets (negative at BER, positive at SOT) was unchanged. Our own JFJ samples were on average 1.2 ± 0.4 ‰ lower than the ICOS background before April 2023 and 1.8 ± 0.9 ‰ lower with the JASS sampling; the difference between the two periods is not significant ($p = 0.57$, Welch t-test).

For $^{14}CH_4$, individual JFJ samples are dominated by episodic nuclear releases that are not resolved by the simulations: 12 of 129 samples deviate from the annual median by more than three robust standard deviations, by up to +376 ‰. The seasonal variation of the nuclear-corrected JFJ values (robust monthly medians between −14 and +9 ‰; not significant for 2022–

https://doi.org/10.5194/egusphere-2026-5725
Preprint. Discussion started: 3 November 2026
© Author(s) 2026. CC BY 4.0 License.

2023, p = 0.25) is comparable to the measurement uncertainty (≈ 11 ‰). We therefore use the annual mean backgrounds of Laemmel et al. (2026). Using annual medians, nuclear-corrected values or interpolated individual samples instead changes the median $\Delta\Delta(^{14}C, CH_4)$ at BER, BRM and SOT by up to 16 ‰; in particular, correcting the JFJ background for its simulated nuclear contribution (6–18 ‰ per year) would raise the median $\Delta\Delta(^{14}C, CH_4)$ by 13–15 ‰. None of these choices affects the conclusions on nuclear contamination and fossil CH_4 apportionment: the three-component fossil CH_4 estimates remain strongly negative (−120 to −385 nmol mol^{-1}) for all background choices.

Table C1: Sensitivity of the nuclear-corrected fossil CO_2 estimates at BER, BRM and SOT (2021–2023) to the background definition. Changes are relative to the baseline B0 (mean, with the per-sample standard deviation of the change in brackets); offsets are the mean corrected ^{14}C-based minus inventory-simulated fossil CO_2.

Variant	Background definition	Change in Δ_{bg} / ‰	Change in fossil CO_2, BER / BRM / SOT (µmol mol^{-1})	Corrected − simulated, BER / BRM / SOT (µmol mol^{-1})
B0	ICOS JFJ two-week integrated, monthly means (baseline)	0	0 / 0 / 0	−3.44 / −0.36 / +0.26
B1	B0 minus simulated nuclear $\Delta\Delta(^{14}C, CO_2)$ at JFJ	−0.3	−0.12 / −0.12 / −0.11 (0.07)	−3.56 / −0.48 / +0.15
B2	Own JFJ samples, interpolated in time	−0.7 to −1.3	−0.31 / −0.30 / −0.56 (1.1–1.2)	−3.74 / −0.66 / −0.29
B3	B2 minus simulated nuclear $\Delta\Delta(^{14}C, CO_2)$	−0.9 to −1.5	−0.38 / −0.37 / −0.64 (1.1–1.2)	−3.82 / −0.73 / −0.38
B4	ICOS, linear trend + annual harmonic fit	−0.2 to +0.2	+0.12 / +0.07 / −0.04 (0.8–1.0)	−3.32 / −0.29 / +0.22
B5	ICOS annual means	≈ 0	0.00 / −0.03 / +0.04 (0.8–0.9)	−3.44 / −0.39 / +0.30
B6	ICOS 3-month running mean	≈ 0	+0.02 / 0.00 / −0.01 (0.5–0.6)	−3.42 / −0.36 / +0.25

https://doi.org/10.5194/egusphere-2026-5725
Preprint. Discussion started: 3 November 2026
© Author(s) 2026. CC BY 4.0 License.

Appendix D: Respiration correction

Table D1: Seasonal respiration correction factors for the biospheric CO_2 flux, calculated using BRM afternoon (12:00 - 15:00 UTC) CO_2 data for the full 2019–2023 study period. R^2 values compare the raw and respiration-corrected simulations against observations. Winter 2018–2019 and winter 2023–2024 are marked with an asterisk, as these periods represent only 3 months of data each and are not discussed further.

Period	Respiration factor	R^2 (raw)	R^2 (corr)
Summer 2019	1.48	0.54	0.59
Summer 2020	1.54	0.44	0.54
Summer 2021	1.64	0.39	0.50
Summer 2022	1.52	0.47	0.58
Summer 2023	1.67	0.49	0.62
*Winter 2018-2019**	0.76	0.72	0.70
Winter 2019-2020	0.98	0.51	0.50
Winter 2020-2021	0.63	0.63	0.66
Winter 2021-2022	1.23	0.67	0.69
Winter 2022-2023	1.22	0.72	0.75
*Winter 2023-2024**	1.14	0.88	0.88

https://doi.org/10.5194/egusphere-2026-5725
Preprint. Discussion started: 3 November 2026
© Author(s) 2026. CC BY 4.0 License.



715 **Figure D1: Time series of afternoon (12:00–15:00 UTC) $y(CO_2)$ at BRM during the summer periods (April–September) of 2019–2023, comparing raw simulated (blue), respiration-corrected simulated (green) and observed (orange) mole fractions. The respiration correction factor was optimized per season-year by least-squares fitting to the observed afternoon CO_2 mole fractions (see Sect. 2.4.4 and Table D1). Dates are aligned to a common calendar year (x axis) to allow direct visual comparison across years.**

https://doi.org/10.5194/egusphere-2026-5725
Preprint. Discussion started: 3 November 2026
© Author(s) 2026. CC BY 4.0 License.

Appendix E: Site-specific model evaluation

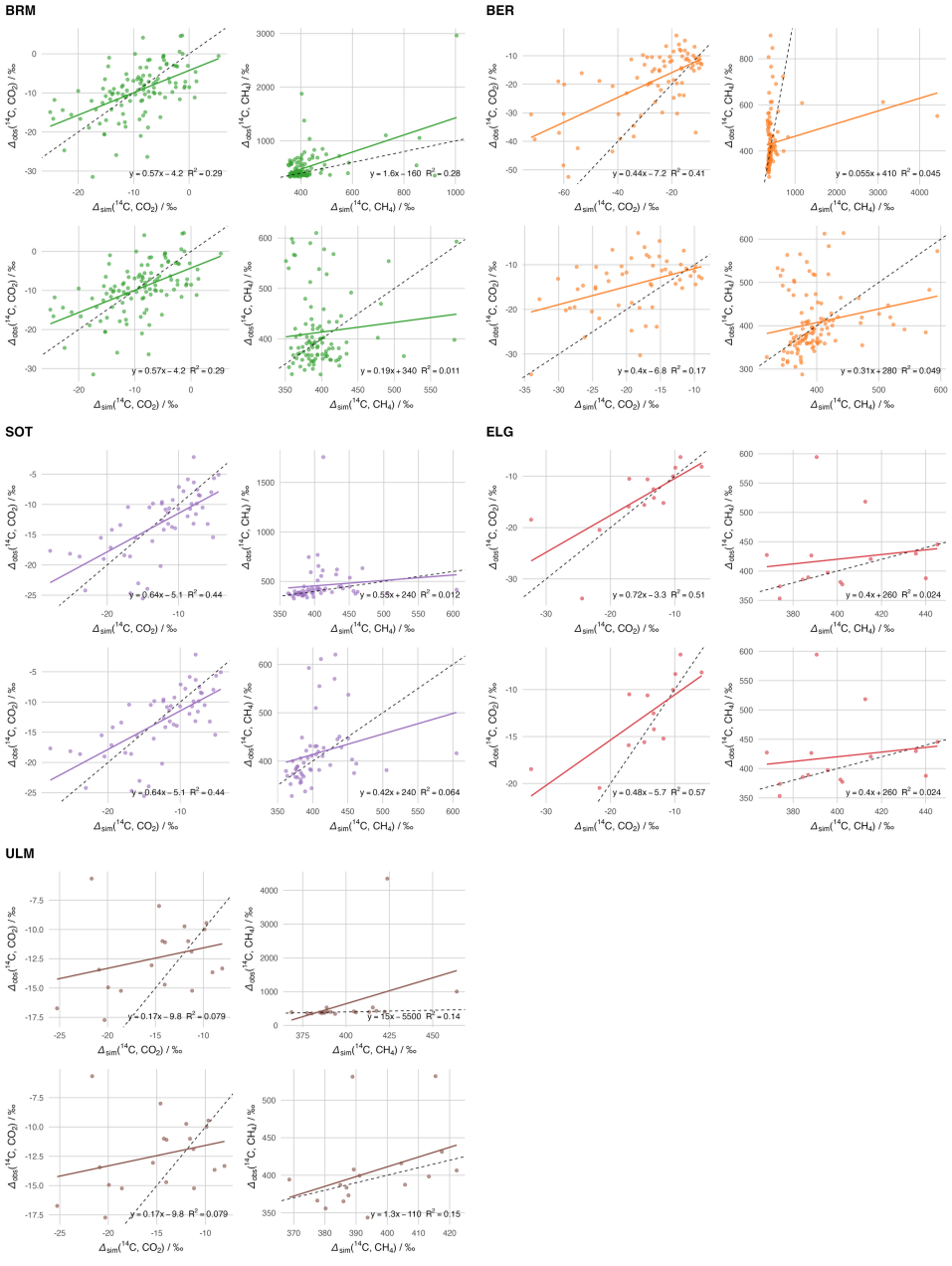


Figure E1: Observed versus simulated $\Delta(^{14}C, CO_2)$ and $\Delta(^{14}C, CH_4)$ at BRM, BER, SOT, ELG and ULM. For each site, the top row shows all samples and the bottom row the zoomed ranges of Fig. 5 ($\Delta\Delta(^{14}C, CO_2) \geq -25$ ‰ and $\Delta\Delta(^{14}C, CH_4) \leq 250$ ‰); simulated values are on the x axis and observed values on the y axis. Dashed lines indicate the 1 : 1 line; solid lines show linear regression fits with their equations and coefficients of determination (R^2). These complement Fig. 5.

https://doi.org/10.5194/egusphere-2026-5725
Preprint. Discussion started: 3 November 2026
© Author(s) 2026. CC BY 4.0 License.

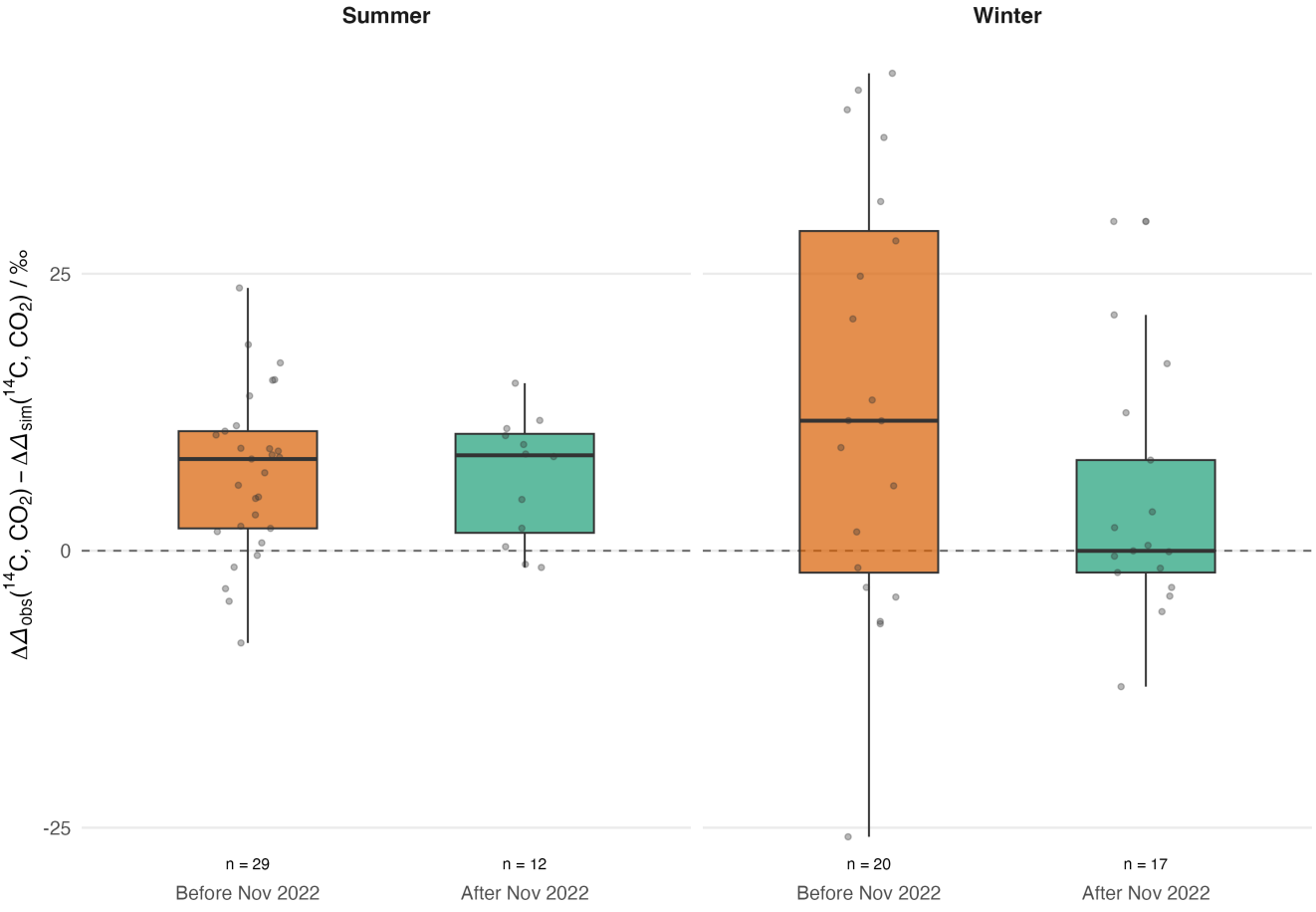


Figure E2: Distribution of the ΔΔ(^{14}C, CO_2) model bias (obs − sim) at BER before and after the November 2022 sampling harmonisation (standardisation to 14:00–15:00 UTC), split by season. Boxes show the median and interquartile range (IQR). The winter bias decreased from +13.7 ± 19.2 ‰ to +3.8 ± 10.7 ‰ after harmonisation, while the summer bias was unaffected (+7.0 vs. +6.6 ‰), consistent with the dominant role of boundary layer stability in setting the morning–afternoon sampling difference.

Appendix F: Fossil CO_2 and CH_4 mass balance

Fossil CO_2 contributions were estimated using the radiocarbon mass balance approach of Turnbull et al. (2006):

$$y_{\mathrm{ff}}(\mathrm{CO_2}) = y(\mathrm{CO_2}) \cdot \frac{\Delta_{\mathrm{bg}} - \Delta_{\mathrm{obs}}}{\Delta_{\mathrm{bg}} - \Delta_{\mathrm{ff}}}$$

where $y(CO_2)$ is the measured CO_2 mole fraction, Δ_{bg} is the monthly mean background value from JFJ (regional atmospheric reference), and Δ_{obs} is the observed $\Delta(^{14}C, CO_2)$ at the measurement site. Here, Δ denotes $\Delta(^{14}C, CO_2)$, and $\Delta_{ff} = -1000$ ‰ is the value of radiocarbon-free fossil carbon. This "raw" estimate assumes all deviation from background is fossil-derived. A nuclear-corrected estimate was obtained by first subtracting the FLEXPART-simulated nuclear $\Delta(^{14}C, CO_2)$ contribution from the observed signal:

https://doi.org/10.5194/egusphere-2026-5725
Preprint. Discussion started: 3 November 2026
© Author(s) 2026. CC BY 4.0 License.

$$\Delta_{\mathrm{corr}} = \Delta_{\mathrm{obs}} - \Delta\Delta_{\mathrm{nuc}}$$

and then applying the same equation with Δ_{corr} in place of Δ_{obs} (Section 2.4.4). An inventory-based fossil CO_2 estimate was computed by weighting each simulated emission sector flux by its fossil carbon fraction (Table B1) and summing across sectors. Figure 8 compares these two ^{14}C-based estimates against the inventory simulation for the three main sites.

BRM shows the closest agreement between the two approaches (Table F1), with the ^{14}C-derived and simulated fossil CO_2 estimates nearly identical on an annual basis (2.42 ± 2.82 vs. 2.78 ± 2.07 µmol mol^{-1}). BER exhibits a larger, seasonally dependent negative offset, most pronounced in winter (−4.16 ± 7.37 µmol mol^{-1}), while SOT shows a small positive winter offset (+1.00 ± 2.01 µmol mol^{-1}). However, the spread (SD) at all three sites is large relative to the magnitude of these offsets, particularly at BER and BRM in winter, so they should not be interpreted as robust evidence of a systematic bias in either direction. The contrasting sign of the winter offset at BER (negative) and SOT (positive) argues against a shared meteorological cause, such as a general misrepresentation of planetary boundary layer height, which would be expected to produce offsets of consistent sign across sites. Instead, site-specific factors are more likely responsible, potentially including the limited ability of the 1 km × 1 km transport model to resolve urban-canopy effects at BER (Section 4.1).

https://doi.org/10.5194/egusphere-2026-5725
Preprint. Discussion started: 3 November 2026
© Author(s) 2026. CC BY 4.0 License.

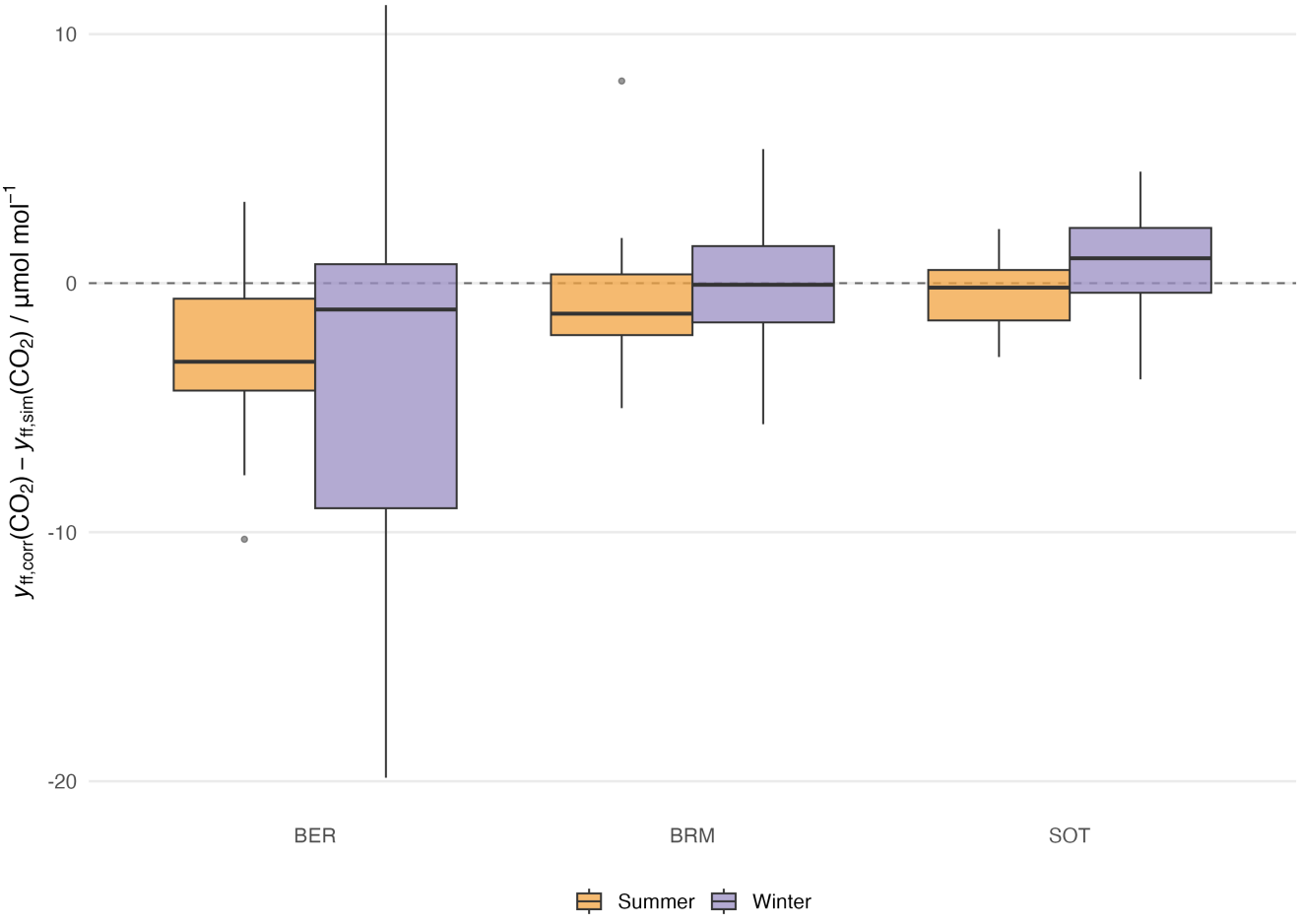


Figure F1: Difference between nuclear-corrected ^{14}C-derived and inventory-simulated fossil CO_2, $y_{ff,corr}(CO_2) - y_{ff,sim}(CO_2)$, at BER, BRM and SOT for 2021–2023, split by season (summer: April–September; winter: October–March). Boxes show the median and IQR; whiskers extend to 1.5 × IQR. Positive values indicate that the ^{14}C mass balance yields more fossil CO_2 than the simulation; negative values indicate the opposite. The dashed line marks zero.

Table F1: Mean difference between nuclear-corrected ^{14}C-derived and inventory-simulated fossil CO_2 (µmol mol^{-1}) at BER, BRM and SOT for the 2021–2023 period, separated by season (summer: April–September; winter: October–March) and overall. Positive values indicate the ^{14}C mass balance yields more fossil CO_2 than the simulation; negative values indicate the opposite

Site	Season	N	Mean offset (µmol mol^{-1})	SD
BER	Summer	41	−2.8	2.8
BER	Winter	37	−4.2	7.4
BER	Annual	78	−3.4	5.5

https://doi.org/10.5194/egusphere-2026-5725
Preprint. Discussion started: 3 November 2026
© Author(s) 2026. CC BY 4.0 License.

BRM	Summer	36	−0.9	2.4
BRM	Winter	38	+0.1	2.5
BRM	Annual	74	−0.4	2.5
SOT	Summer	26	−0.5	1.5
SOT	Winter	27	+1.0	2.0
SOT	Annual	53	+0.3	1.9

An equivalent source apportionment analysis to that performed for CO_2 (Fig. 8) was attempted for CH_4 using the same three approaches: raw $^{14}CH_4$-based mass balance, nuclear-corrected mass balance, and inventory-based simulations (Fig. F2). Because biogenic CH_4 ($\Delta(^{14}C) \approx -9$ ‰, Table B1) is strongly depleted relative to the CH_4 background ($\Delta(^{14}C) \approx 360$–$380$ ‰), a three-component mass balance (background, biogenic, fossil) was used instead of the two-component form applied to CO_2: $y_{ff}(CH_4) = [y_{bg}(CH_4) \cdot (\Delta_{bg} - \Delta_{bio}) - y(CH_4) \cdot (\Delta_{obs} - \Delta_{bio})] / (\Delta_{bio} - \Delta_{ff})$, where Δ denotes $\Delta(^{14}C, CH_4)$, $\Delta_{bio} = -9$ ‰, $\Delta_{ff} = -1000$ ‰, Δ_{bg} is the JFJ background and $y_{bg}(CH_4)$ the simulated background mole fraction. The nuclear-corrected estimate uses Δ_{obs} minus the simulated nuclear contribution from all Swiss and European sources.

Unlike the successful $^{14}CO_2$ apportionment, nuclear correction of $^{14}CH_4$ led to severe overcorrection, yielding physically implausible negative fossil CH_4 estimates at numerous time points. This failure results from the inability of monthly/quarterly emission inventories to resolve sporadic PWR $^{14}CH_4$ releases, which can occur over hours to days during maintenance outages (Espic et al., 2025). The resulting temporal smearing causes systematic underprediction of nuclear peaks and overprediction during quiescent periods. When these biased corrections are applied, the residual signal is misattributed to biogenic sources, driving fossil fractions to negative values.

https://doi.org/10.5194/egusphere-2026-5725
Preprint. Discussion started: 3 November 2026
© Author(s) 2026. CC BY 4.0 License.



Figure F2: Fossil CH_4 contributions at BER, BRM and SOT from the raw ^{14}C mass balance (red), the nuclear-corrected mass balance (green) and the transport simulations (dashed blue). Grey shading indicates winter months. The raw ^{14}C mass balance and the nuclear correction yield physically implausible fossil CH_4 values at multiple time points, demonstrating the failure of $^{14}CH_4$-based source apportionment in nuclear-influenced regions (see Sects. 3.4 and 4.3). The y axis is limited to −1000 to 500 nmol mol^{-1}; values outside this range are clipped (raw ^{14}C: 2, 4 and 1 samples; corrected ^{14}C: 1, 3 and 1 samples at BER, BRM and SOT, respectively).

https://doi.org/10.5194/egusphere-2026-5725
Preprint. Discussion started: 3 November 2026
© Author(s) 2026. CC BY 4.0 License.

Code/Data availability

The observational data, processed model-observation datasets, and analysis scripts supporting this study are archived on Zenodo (https://doi.org/10.5281/zenodo.22846899), under a under a Creative Commons Attribution 4.0 International license and will be made publicly available upon acceptance.

Author contributions

DG: Conceptualization, Data curation, Formal analysis, Investigation, Methodology, Project administration, Software, Validation, Visualization, Writing – original draft, Writing – review and editing. TL: Conceptualization, Data curation, Formal analysis, Investigation, Methodology, Project administration, Software, Validation, Visualization, Writing – original draft, Writing – review and editing. SH: Investigation Methodology, Software, Validation, Visualization, Writing – original draft, Writing –review and editing. DB: Investigation, Writing – review and editing. NH: Investigation. PG: Investigation, Methodology. ML: Investigation, Writing – review and editing. CE: Data curation. MB: Data curation, Writing – review and editing. HG: Supervision, Writing – original draft, Writing – review and editing. LW: Conceptualization, Investigation, Resources, Supervision, Writing-review and editing. SS: Conceptualization, Funding acquisition, Project administration, Resources, Supervision, Writing – review and editing.

Competing Interests

The corresponding author has declared that none of the authors has any competing interests.

Acknowledgements

We are grateful to the funding of the SNSF Sinergia project n°193770 (Radiocarbon Inventories of Switzerland – RICH: integrated approach to understand the changing carbon cycle) as well as the Dr. Alfred Bretscher Scholarship. We thank the members of the workshop at the Department of Chemistry, Biochemistry and Pharmaceutical Sciences, as well as René Schraner and René Bleisch for their help in developing the different sampling devices. We would like to thank the International Foundation High Altitude Research Stations Jungfraujoch and Gornergrat (HFSJG), for enabling us to carry out our experiments at the Jungfraujoch High Altitude Research Station and the Jungfraujoch's custodians (Joan & Martin Fischer, Christine & Ruedi Käser, Daniela Bissig & Erich Furrer, and Sonja Stöckli & Thomas Furter) for their support on site. We thank as well: Rüdiger Schanda for collecting the initial air samples at BRM, Christoph Zellweger for his help to calibrate our three standard bottles against the NOAA calibration scale, Céline Pascale and Tobias Bühlmann (METAS) for the possibility to use their CRDS analyser for gas concentration measurements, Swisscom for the access to the ELG and ULM tall towers and the installation of the sampling lines there, Gecko for granting access to the SOT tall tower and Pascal

https://doi.org/10.5194/egusphere-2026-5725
Preprint. Discussion started: 3 November 2026
© Author(s) 2026. CC BY 4.0 License.

Rubli for allowing us to share the sampling line there as well as for sharing their SOT *in-situ* CO_2 measurements. We finally thank the staff of the nuclear power plant Paks (Hungary) for sharing their ^{14}C emission data that we used in the atmospheric ^{14}C modelling and Mihály Molnár for the communication with them.

AI tools were used for text formatting help, and code writing/correction, but all analyses and interpretations were made by the authors.

Financial support

This research has been supported by the Schweizerischer Nationalfonds zur Förderung der Wissenschaftlichen Forschung (grant nos. 193770, 20FI20_173691, 20FI20_198227, and 20FI-0_229655).

References

Basu, S., Lehman, S. J., Miller, J. B., Andrews, A. E., Sweeney, C., Gurney, K. R., Xu, X., Southon, J., and Tans, P. P.: Estimating US fossil fuel CO_2 emissions from measurements of^{14} C in atmospheric CO_2, Proc. Natl. Acad. Sci. U.S.A., 117, 13300–13307, https://doi.org/10.1073/pnas.1919032117, 2020.

Basu, S., Lan, X., Dlugokencky, E., Michel, S., Schwietzke, S., Miller, J. B., Bruhwiler, L., Oh, Y., Tans, P. P., Apadula, F., Gatti, L. V., Jordan, A., Necki, J., Sasakawa, M., Morimoto, S., Di Iorio, T., Lee, H., Arduini, J., and Manca, G.: Estimating Emissions of Methane Consistent with Atmospheric Measurements of Methane and δ^{13} C of Methane, https://doi.org/10.5194/acp-2022-317, 5 July 2022., 2022.

Berhanu, T. A., Satar, E., Schanda, R., Nyfeler, P., Moret, H., Brunner, D., Oney, B., and Leuenberger, M.: Measurements of greenhouse gases at Beromünster tall-tower station in Switzerland, Atmos. Meas. Tech., 9, 2603–2614, https://doi.org/10.5194/amt-9-2603-2016, 2016.

Berhanu, T. A., Szidat, S., Brunner, D., Satar, E., Schanda, R., Nyfeler, P., Battaglia, M., Steinbacher, M., Hammer, S., and Leuenberger, M.: Estimation of the fossil fuel component in atmospheric CO_2 based on radiocarbon measurements at the Beromünster tall tower, Switzerland, Atmos. Chem. Phys., 2017.

Biofuels-Schweiz: Biotreibstoffe - Verband Biofuels Schweiz, https://www.biosprit.org/biotreibstoffe/, last access: 3 February 2025, 2025., 2025.

Byrd, R. H., Lu, P., Nocedal, J., and Zhu, C.: A limited memory algorithm for bound constrained optimization, SIAM J. Sci. Comput., 16, 1190–1208, https://doi.org/10.1137/0916069, 1995.

Calvin, K., Dasgupta, D., Krinner, G., Mukherji, A., Thorne, P. W., Trisos, C., Romero, J., Aldunce, P., Barrett, K., Blanco, G., Cheung, W. W. L., Connors, S., Denton, F., Diongue-Niang, A., Dodman, D., Garschagen, M., Geden, O., Hayward, B., Jones, C., Jotzo, F., Krug, T., Lasco, R., Lee, Y.-Y., Masson-Delmotte, V., Meinshausen, M., Mintenbeck, K., Mokssit, A., Otto, F. E. L., Pathak, M., Pirani, A., Poloczanska, E., Pörtner, H.-O., Revi, A., Roberts, D. C., Roy, J., Ruane, A. C., Skea,

https://doi.org/10.5194/egusphere-2026-5725
Preprint. Discussion started: 3 November 2026
© Author(s) 2026. CC BY 4.0 License.

J., Shukla, P. R., Slade, R., Slangen, A., Sokona, Y., Sörensson, A. A., Tignor, M., Van Vuuren, D., Wei, Y.-M., Winkler, H., Zhai, P., Zommers, Z., Hourcade, J.-C., Johnson, F. X., Pachauri, S., Simpson, N. P., Singh, C., Thomas, A., Totin, E., Alegría, A., Armour, K., Bednar-Friedl, B., Blok, K., Cissé, G., Dentener, F., Eriksen, S., Fischer, E., Garner, G., Guivarch, C., Haasnoot, M., Hansen, G., Hauser, M., Hawkins, E., Hermans, T., Kopp, R., Leprince-Ringuet, N., Lewis, J., Ley, D., Ludden, C., Niamir, L., Nicholls, Z., Some, S., Szopa, S., Trewin, B., Van Der Wijst, K.-I., Winter, G., Witting, M., Birt, A., and Ha, M.: IPCC, 2023: Climate Change 2023: Synthesis Report. Contribution of Working Groups I, II and III to the Sixth Assessment Report of the Intergovernmental Panel on Climate Change [Core Writing Team, H. Lee and J. Romero (eds.)]. IPCC, Geneva, Switzerland., Intergovernmental Panel on Climate Change (IPCC), https://doi.org/10.59327/IPCC/AR6-9789291691647, 2023.

CARBURA: Geschäftsbericht 2022, CARBURA – Schweizerische Pflichtlagerorganisation für flüssige Treib- und Brennstoffe, Zürich, https://www.carbura.ch/fileadmin/user_upload/editors/web_dokumente/pdf_dokumente/Geschaeftsberichte/2022_Carbura_GB_DE.pdf (last access: 11 September 2026), 2023.

cemsuisse: Rapport annuel cemsuisse, cemsuisse, report2024.cemsuisse.ch/fr (last access: 29 October 2024), 2024.

Conen, F. and Zimmermann, L.: Separating “free tropospheric conditions” from those “influenced by the planetary boundary layer,” HFSJG Annual Report, 2020.

Eisma, R., Van Der Borg, K., De Jong, A. F. M., Kieskamp, W. M., and Veltkamp, A. C.: Measurements of the 14C content of atmospheric methane in The Netherlands to determine the regional emissions of 14CH4, Nuclear Instruments and Methods in Physics Research Section B: Beam Interactions with Materials and Atoms, 92, 410–412, https://doi.org/10.1016/0168-583X(94)96044-5, 1994.

Eisma, R., Vermeulen, A. T., and Van Der Borg, K.: $^{14}CH_4$ Emissions from Nuclear Power Plants in Northwestern Europe, Radiocarbon, 37, 475–483, https://doi.org/10.1017/S0033822200030952, 1995.

Emmenegger, L., Leuenberger, M., and Steinbacher, M.: ICOS ATC ^{14}C Release analysed by ICOS CRL, Jungfraujoch (6.0 m), 2015-09-21–2023-10-02, 2024a.

Emmenegger, L., Leuenberger, M., and Steinbacher, M.: ICOS ATC CO_2 Release, Jungfraujoch (13.9 m), 2016-12-12–2024-03-31, 2024b.

Emmenegger, L., Leuenberger, M., and Steinbacher, M.: ICOS ATC NRT CH_4 growing time series, Jungfraujoch (13.9 m), 2024-04-01–2025-02-01, 2025.

Espic, C., Liechti, M., Battaglia, M., Paul, D., Röckmann, T., and Szidat, S.: Compound-Specific Radiocarbon Analysis of Atmospheric Methane: A New Preconcentration and Purification Setup, Radiocarbon, 61, 1461–1476, https://doi.org/10.1017/RDC.2019.76, 2019.

Espic, C., Laemmel, T., Henne, S., Purtschert, R., and Szidat, S.: Atmospheric 14CH4, 14CO2 and 37Ar measurements around a Swiss pressurized water reactor during an annual revision period, Journal of Environmental Radioactivity, 281, 107576, https://doi.org/10.1016/j.jenvrad.2024.107576, 2025.

https://doi.org/10.5194/egusphere-2026-5725
Preprint. Discussion started: 3 November 2026
© Author(s) 2026. CC BY 4.0 License.

FOEN, F. O. for the E.: Switzerland's Greenhouse Gas Inventory 1990–2022, United Nations Framework Convention on Climate Change., 2024, Federal Office for the Environment, Bern, 2024.

FOEN, F. O. for the E.: Switzerland's National Inventory Document 2026 (GHG inventory 1990-2024), 2026.

FSO: Land use and land cover, Swiss Federal Statistical Office, https://www.bfs.admin.ch/content/bfs/en/home/statistics/territory-environment/land-use-cover.html (last access: 11 September 2026), 2026.

Fujita, R., Graven, H., Zazzeri, G., Hmiel, B., Petrenko, V. V., Smith, A. M., Michel, S. E., and Morimoto, S.: Global Fossil Methane Emissions Constrained by Multi-Isotopic Atmospheric Methane Histories, JGR Atmospheres, 130, e2024JD041266, https://doi.org/10.1029/2024JD041266, 2025.

Gautschi, P.: A new method to graphitize CO2 from atmospheric air for radiocarbon analysis, Master Thesis, 2017.

Gazenergie-Verband der Schweiz, G.-V. der S.: Gazenergie-Verband der Schweiz, https://gazenergie.ch/de/verband/news/detail/gasabsatz-wird-immer-staerker-erneuerbar, last access: 14 January 2026, 2023., 2023.

Geissbühler, D., Laemmel, T., Antoni, M., Gautschi, P., Wacker, L., and Szidat, S.: Verification of fossil CO2 emissions from Swiss cement factories using direct and indirect 14CO2 measurements, Atmospheric Environment: X, 27, 100349, https://doi.org/10.1016/j.aeaoa.2025.100349, 2025.

Genoud, G., Lehmuskoski, J., Bell, S., Palonen, V., Oinonen, M., Koskinen-Soivi, M.-L., and Reinikainen, M.: Laser Spectroscopy for Monitoring of Radiocarbon in Atmospheric Samples, Anal. Chem., 91, 12315–12320, https://doi.org/10.1021/acs.analchem.9b02496, 2019.

Gómez-Ortiz, C., Monteil, G., Basu, S., and Scholze, M.: A CO_2 –Δ^{14} CO_2 inversion setup for estimating European fossil CO_2 emissions, Atmos. Chem. Phys., 25, 397–424, https://doi.org/10.5194/acp-25-397-2025, 2025.

Gourdji, S. M., Karion, A., Lopez-Coto, I., Ghosh, S., Mueller, K. L., Zhou, Y., Williams, C. A., Baker, I. T., Haynes, K. D., and Whetstone, J. R.: A Modified Vegetation Photosynthesis and Respiration Model (VPRM) for the Eastern USA and Canada, Evaluated With Comparison to Atmospheric Observations and Other Biospheric Models, JGR Biogeosciences, 127, e2021JG006290, https://doi.org/10.1029/2021JG006290, 2022.

Grange, S. K., Rubli, P., Fischer, A., Brunner, D., Hueglin, C., and Emmenegger, L.: The ZiCOS-M CO_2 sensor network: measurement performance and CO_2 variability across Zürich, https://doi.org/10.5194/egusphere-2024-2925, 21 October 2024., 2024.

Graven, H., Fischer, M. L., Lueker, T., Jeong, S., Guilderson, T. P., Keeling, R. F., Bambha, R., Brophy, K., Callahan, W., Cui, X., Frankenberg, C., Gurney, K. R., LaFranchi, B. W., Lehman, S. J., Michelsen, H., Miller, J. B., Newman, S., Paplawsky, W., Parazoo, N. C., Sloop, C., and Walker, S. J.: Assessing fossil fuel CO_2 emissions in California using atmospheric observations and models, Environ. Res. Lett., 13, 065007, https://doi.org/10.1088/1748-9326/aabd43, 2018.

Graven, H., Hocking, T., and Zazzeri, G.: Detection of Fossil and Biogenic Methane at Regional Scales Using Atmospheric Radiocarbon, Earth's Future, 7, 283–299, https://doi.org/10.1029/2018EF001064, 2019.

https://doi.org/10.5194/egusphere-2026-5725
Preprint. Discussion started: 3 November 2026
© Author(s) 2026. CC BY 4.0 License.

Graven, H. D., Warren, H., Gibbs, H. K., Khatiwala, S., Koven, C., Lester, J., Levin, I., Spawn-Lee, S. A., and Wieder, W.: Bomb radiocarbon evidence for strong global carbon uptake and turnover in terrestrial vegetation, Science, 384, 1335–1339, https://doi.org/10.1126/science.adl4443, 2024.

Haghnegahdar, M. A., Sun, J., Hultquist, N., Hamovit, N. D., Kitchen, N., Eiler, J., Ono, S., Yarwood, S. A., Kaufman, A. J., Dickerson, R. R., Bouyon, A., Magen, C., and Farquhar, J.: Tracing sources of atmospheric methane using clumped isotopes, Proc. Natl. Acad. Sci. U.S.A., 120, e2305574120, https://doi.org/10.1073/pnas.2305574120, 2023.

Heldstab, J., Schäppi, B., and Künzle, T.: Treibhausgase und Luftschadstoffe, BAFU, Infras, Zurich/Bern, 2021.

Henne, S., Brunner, D., Folini, D., Solberg, S., Klausen, J., and Buchmann, B.: Assessment of parameters describing representativeness of air quality in-situ measurement sites, Atmos. Chem. Phys., 10, 3561–3581, https://doi.org/10.5194/acp-10-3561-2010, 2010.

Henne, S., Brunner, D., Oney, B., Leuenberger, M., Eugster, W., Bamberger, I., Meinhardt, F., Steinbacher, M., and Emmenegger, L.: Validation of the Swiss methane emission inventory by atmospheric observations and inverse modelling, Atmos. Chem. Phys., 16, 3683–3710, https://doi.org/10.5194/acp-16-3683-2016, 2016.

Herrmann, E., Weingartner, E., Henne, S., Vuilleumier, L., Bukowiecki, N., Steinbacher, M., Conen, F., Collaud Coen, M., Hammer, E., Jurányi, Z., Baltensperger, U., and Gysel, M.: Analysis of long-term aerosol size distribution data from Jungfraujoch with emphasis on free tropospheric conditions, cloud influence, and air mass transport, JGR Atmospheres, 120, 9459–9480, https://doi.org/10.1002/2015JD023660, 2015.

Hiller, R. V., Bretscher, D., DelSontro, T., Diem, T., Eugster, W., Henneberger, R., Hobi, S., Hodson, E., Imer, D., Kreuzer, M., Künzle, T., Merbold, L., Niklaus, P. A., Rihm, B., Schellenberger, A., Schroth, M. H., Schubert, C. J., Siegrist, H., Stieger, J., Buchmann, N., and Brunner, D.: Anthropogenic and natural methane fluxes in Switzerland synthesized within a spatially explicit inventory, Biogeosciences, 11, 1941–1959, https://doi.org/10.5194/bg-11-1941-2014, 2014.

Hua, Q., Turnbull, J. C., Santos, G. M., Rakowski, A. Z., Ancapichún, S., De Pol-Holz, R., Hammer, S., Lehman, S. J., Levin, I., Miller, J. B., Palmer, J. G., and Turney, C. S. M.: ATMOSPHERIC RADIOCARBON FOR THE PERIOD 1950–2019, Radiocarbon, 64, 723–745, https://doi.org/10.1017/RDC.2021.95, 2022.

IAEA PRIS: Power Reactor Information System (PRIS), http://www.iaea.org/resources/databases/power-reactor-information-system-pris, last access: 21 February 2026, 2025., 2025.

Jähn, M., Kuhlmann, G., Mu, Q., Haussaire, J.-M., Ochsner, D., Osterried, K., Clément, V., and Brunner, D.: An online emission module for atmospheric chemistry transport models: implementation in COSMO-GHG v5.6a and COSMO-ART v5.1-3.1, Geosci. Model Dev., 13, 2379–2392, https://doi.org/10.5194/gmd-13-2379-2020, 2020.

Katharopoulos, I., Brunner, D., Emmenegger, L., Leuenberger, M., and Henne, S.: Lagrangian Particle Dispersion Models in the Grey Zone of Turbulence: Adaptations to FLEXPART-COSMO for Simulations at 1 km Grid Resolution, Boundary-Layer Meteorol, 185, 129–160, https://doi.org/10.1007/s10546-022-00728-3, 2022.

Katharopoulos, I., Rust, D., Vollmer, M. K., Brunner, D., Reimann, S., O'Doherty, S. J., Young, D., Stanley, K. M., Schuck, T., Arduini, J., Emmenegger, L., and Henne, S.: Impact of transport model resolution and a priori assumptions on inverse

https://doi.org/10.5194/egusphere-2026-5725
Preprint. Discussion started: 3 November 2026
© Author(s) 2026. CC BY 4.0 License.

modeling of Swiss F-gas emissions, Atmos. Chem. Phys., 23, 14159–14186, https://doi.org/10.5194/acp-23-14159-2023, 2023.

Kretschmer, R., Gerbig, C., Karstens, U., and Koch, F.-T.: Error characterization of CO_2 vertical mixing in the atmospheric transport model WRF-VPRM, Atmos. Chem. Phys., 12, 2441–2458, https://doi.org/10.5194/acp-12-2441-2012, 2012.

Kuenen, J., Dellaert, S., Visschedijk, A., Jalkanen, J.-P., Super, I., and Denier Van Der Gon, H.: CAMS-REG-v4: a state-of-the-art high-resolution European emission inventory for air quality modelling, Earth Syst. Sci. Data, 14, 491–515, https://doi.org/10.5194/essd-14-491-2022, 2022.

Kunz, C.: Carbon-14 Discharge at Three Light-water Reactors:, Health Physics, 49, 25–35, https://doi.org/10.1097/00004032-198507000-00002, 1985.

Kutschera, W.: The Half-Life of^{14} C—Why Is It So Long?, Radiocarbon, 61, 1135–1142, https://doi.org/10.1017/RDC.2019.26, 2019.

Laemmel, T., Knaack, T., Heckel, A., Xue, G., Wenger, A., Zazzeri, G., Fujita, R., Graven, H., and Szidat, S.: Inventory of the nuclear gaseous $^{14}CO_2$ and $^{14}CH_4$ Emissions from 1970 to 2023, 2025., 2025.

Laemmel, T., Geissbühler, D., Henne, S., Fujita, R., Graven, H., Espic, C., Bantle, M., Haghipour, N., Conen, F., Brunner, D., Steinbacher, M., Zazzeri, G., Hammer, S., Leuenberger, M., and Szidat, S.: Radiocarbon in atmospheric CH_4 and CO_2 at Jungfraujoch in 2019–2024: influence of regional nuclear emissions and current global atmospheric^{14} CH_4 signal, Atmos. Chem. Phys., 26, 12019–12036, https://doi.org/10.5194/acp-26-12019-2026, 2026.

Lehmuskoski, J., Vasama, H., Hämäläinen, J., Hokkinen, J., Kärkelä, T., Heiskanen, K., Reinikainen, M., Rautio, S., Hirvelä, M., and Genoud, G.: On-Line Monitoring of Radiocarbon Emissions in a Nuclear Facility with Cavity Ring-Down Spectroscopy, Anal. Chem., 2021.

Levin, I., Bösinger, R., Bonani, G., Francey, R. J., Kromer, B., Münnich, K. O., Suter, M., Trivett, N. B. A., and Wölfli, W.: Radiocarbon in Atmospheric Carbon Dioxide and Methane: Global Distribution and Trends, in: Radiocarbon After Four Decades, edited by: Taylor, R. E., Long, A., and Kra, R. S., Springer New York, New York, NY, 503–518, https://doi.org/10.1007/978-1-4757-4249-7_31, 1992.

Levin, I., Hammer, S., Kromer, B., Preunkert, S., Weller, R., and Worthy, D. E.: Radiocarbon in Global Tropospheric Carbon Dioxide, Radiocarbon, 64, 781–791, https://doi.org/10.1017/RDC.2021.102, 2022.

Mahadevan, P., Wofsy, S. C., Matross, D. M., Xiao, X., Dunn, A. L., Lin, J. C., Gerbig, C., Munger, J. W., Chow, V. Y., and Gottlieb, E. W.: A satellite-based biosphere parameterization for net ecosystem CO_2 exchange: Vegetation Photosynthesis and Respiration Model (VPRM), Global Biogeochemical Cycles, 22, 2006GB002735, https://doi.org/10.1029/2006GB002735, 2008.

Malardel, S., Wedi, N., Deconinck, W., Diamantakis, M., Kuehnlein, C., Mozdzynski, G., Hamrud, M., and Smolarkiewicz, P.: A new grid for the IFS, https://doi.org/10.21957/ZWDU9U5I, 2016.

https://doi.org/10.5194/egusphere-2026-5725
Preprint. Discussion started: 3 November 2026
© Author(s) 2026. CC BY 4.0 License.

Miller, J. B., Lehman, S. J., Montzka, S. A., Sweeney, C., Miller, B. R., Karion, A., Wolak, C., Dlugokencky, E. J., Southon, J., Turnbull, J. C., and Tans, P. P.: Linking emissions of fossil fuel CO_2 and other anthropogenic trace gases using atmospheric $^{14}CO_2$, J. Geophys. Res., 117, 2011JD017048, https://doi.org/10.1029/2011JD017048, 2012.

Minich, L. I., Geissbühler, D., Tobler, S., Udke, A., Brunmayr, A. S., Moreno Duborgel, M., McMackin, C., Wacker, L., Gautschi, P., Haghipour, N., Egli, M., Kahmen, A., Leifeld, J., Eglinton, T. I., and Hagedorn, F.: Conceptualising carbon cycling pathways across different land-use types based on rates and ages of soil-respired CO_2, Biogeosciences, 23, 811–829, https://doi.org/10.5194/bg-23-811-2026, 2026.

Mohn, J., Szidat, S., Fellner, J., Rechberger, H., Quartier, R., Buchmann, B., and Emmenegger, L.: Determination of biogenic and fossil CO_2 emitted by waste incineration based on $^{14}CO_2$ and mass balances, Bioresource Technology, 99, 6471–6479, https://doi.org/10.1016/j.biortech.2007.11.042, 2008.

Mohn, J., Szidat, S., Zeyer, K., and Emmenegger, L.: Fossil and biogenic CO_2 from waste incineration based on a yearlong radiocarbon study, Waste Management, 32, 1516–1520, https://doi.org/10.1016/j.wasman.2012.04.002, 2012.

NFI: Topics by conifers and broadleaves, Swiss National Forest Inventory, opendata.swiss, https://opendata.swiss/en/dataset/lfi-themen-nach-nadel-und-laubholz (last access: 11 September 2026), 2026.

Oney, B., Henne, S., Gruber, N., Leuenberger, M., Bamberger, I., Eugster, W., and Brunner, D.: The CarboCount CH sites: characterization of a dense greenhouse gas observation network, Atmos. Chem. Phys., 15, 11147–11164, https://doi.org/10.5194/acp-15-11147-2015, 2015.

Pieber, S. M., Tuzson, B., Henne, S., Karstens, U., Gerbig, C., Koch, F.-T., Brunner, D., Steinbacher, M., and Emmenegger, L.: Analysis of regional CO_2 contributions at the high Alpine observatory Jungfraujoch by means of atmospheric transport simulations and $\delta^{13}C$, Atmos. Chem. Phys., 22, 10721–10749, https://doi.org/10.5194/acp-22-10721-2022, 2022.

Pisso, I., Sollum, E., Grythe, H., Kristiansen, N. I., Cassiani, M., Eckhardt, S., Arnold, D., Morton, D., Thompson, R. L., Groot Zwaaftink, C. D., Evangeliou, N., Sodemann, H., Haimberger, L., Henne, S., Brunner, D., Burkhart, J. F., Fouilloux, A., Brioude, J., Philipp, A., Seibert, P., and Stohl, A.: The Lagrangian particle dispersion model FLEXPART version 10.4, Geosci. Model Dev., 12, 4955–4997, https://doi.org/10.5194/gmd-12-4955-2019, 2019.

Ramsperger, U., De Maria, D., Gautschi, P., Maxeiner, S., Müller, A. M., Synal, H.-A., and Wacker, L.: LEA—A novel low energy accelerator for ^{14}C dating, Radiocarbon, 1–9, https://doi.org/10.1017/RDC.2023.85, 2023.

Röckmann, T., Eyer, S., Van Der Veen, C., Popa, M. E., Tuzson, B., Monteil, G., Houweling, S., Harris, E., Brunner, D., Fischer, H., Zazzeri, G., Lowry, D., Nisbet, E. G., Brand, W. A., Necki, J. M., Emmenegger, L., and Mohn, J.: In situ observations of the isotopic composition of methane at the Cabauw tall tower site, Atmos. Chem. Phys., 16, 10469–10487, https://doi.org/10.5194/acp-16-10469-2016, 2016.

Ruff, M., Wacker, L., Gäggeler, H. W., Suter, M., Synal, H.-A., and Szidat, S.: A Gas Ion Source for Radiocarbon Measurements at 200 kV, Radiocarbon, 49, 307–314, https://doi.org/10.1017/S0033822200042235, 2007.

https://doi.org/10.5194/egusphere-2026-5725
Preprint. Discussion started: 3 November 2026
© Author(s) 2026. CC BY 4.0 License.

Satar, E., Berhanu, T. A., Brunner, D., Henne, S., and Leuenberger, M.: Continuous CO2/CH4/CO measurements (2012–2014) at Beromünster tall tower station in Switzerland, Biogeosciences, 13, 2623–2635, https://doi.org/10.5194/bg-13-2623-2016, 2016.

Schuur, E. A. G., Druffel, E., and Trumbore, S. E. (Eds.): Radiocarbon and Climate Change, Springer International Publishing, Cham, https://doi.org/10.1007/978-3-319-25643-6, 2016.

Stenström, K., Erlandsson, B., Hellborg, R., Wiebert, A., Skog, S., Vesanen, R., Alpsten, M., and Bjurman, B.: A one-year study of the total air-borne14C effluents from two Swedish light-water reactors, one boiling water- and one pressurized water reactor, Journal of Radioanalytical and Nuclear Chemistry, Articles, 198, 203–213, https://doi.org/10.1007/BF02038258, 1995.

Stuiver, M. and Polach, H. A.: Discussion Reporting of ^{14}C Data, Radiocarbon, 19, 355–363, https://doi.org/10.1017/S0033822200003672, 1977.

SwissPRTR: SwissPRTR pollutant register, https://www.bafu.admin.ch/bafu/en/home/themen/thema-chemikalien/chemikalien--daten--indikatoren-und-karten/schadstoffregister-swissprtr.html, last access: 1 October 2024, 2024., 2024.

Synal, H.-A., Stocker, M., and Suter, M.: MICADAS: A new compact radiocarbon AMS system, Nuclear Instruments and Methods in Physics Research Section B: Beam Interactions with Materials and Atoms, 259, 7–13, https://doi.org/10.1016/j.nimb.2007.01.138, 2007.

Turnbull, J. C., Miller, J. B., Lehman, S. J., Tans, P. P., Sparks, R. J., and Southon, J.: Comparison of^{14} CO_2 , CO, and SF_6 as tracers for recently added fossil fuel CO_2 in the atmosphere and implications for biological CO_2 exchange, Geophysical Research Letters, 33, 2005GL024213, https://doi.org/10.1029/2005GL024213, 2006.

Turnbull, J. C., Keller, E. D., Baisden, T., Brailsford, G., Bromley, T., Norris, M., and Zondervan, A.: Atmospheric measurement of point source fossil CO_2 emissions, Atmos. Chem. Phys., 14, 5001–5014, https://doi.org/10.5194/acp-14-5001-2014, 2014.

Turnbull, J. C., Karion, A., Davis, K. J., Lauvaux, T., Miles, N. L., Richardson, S. J., Sweeney, C., McKain, K., Lehman, S. J., Gurney, K. R., Patarasuk, R., Liang, J., Shepson, P. B., Heimburger, A., Harvey, R., and Whetstone, J.: Synthesis of Urban CO_2 Emission Estimates from Multiple Methods from the Indianapolis Flux Project (INFLUX), Environ. Sci. Technol., 53, 287–295, https://doi.org/10.1021/acs.est.8b05552, 2019.

Van Der Laan, S., Van Der Laan-Luijkx, I. T., Zimmermann, L., Conen, F., and Leuenberger, M.: Net CO_2 surface emissions at Bern, Switzerland inferred from ambient observations of CO_2 , $\delta(O_2/N_2)$, and^{222} Rn using a customized radon tracer inversion, JGR Atmospheres, 119, 1580–1591, https://doi.org/10.1002/2013JD020307, 2014.

Wacker, L., Němec, M., and Bourquin, J.: A revolutionary graphitisation system: Fully automated, compact and simple, Nuclear Instruments and Methods in Physics Research Section B: Beam Interactions with Materials and Atoms, 268, 931–934, https://doi.org/10.1016/j.nimb.2009.10.067, 2010a.

https://doi.org/10.5194/egusphere-2026-5725
Preprint. Discussion started: 3 November 2026
© Author(s) 2026. CC BY 4.0 License.

Wacker, L., Christl, M., and Synal, H.-A.: Bats: A new tool for AMS data reduction, Nuclear Instruments and Methods in Physics Research Section B: Beam Interactions with Materials and Atoms, 268, 976–979, https://doi.org/10.1016/j.nimb.2009.10.078, 2010b.

Wacker, L., Bonani, G., Friedrich, M., Hajdas, I., Kromer, B., Němec, M., Ruff, M., Suter, M., Synal, H.-A., and Vockenhuber, C.: MICADAS: Routine and High-Precision Radiocarbon Dating, Radiocarbon, 52, 252–262, https://doi.org/10.1017/S0033822200045288, 2010c.

Wacker, L., Fahrni, S. M., Hajdas, I., Molnar, M., Synal, H.-A., Szidat, S., and Zhang, Y. L.: A versatile gas interface for routine radiocarbon analysis with a gas ion source, Nuclear Instruments and Methods in Physics Research Section B: Beam Interactions with Materials and Atoms, 294, 315–319, https://doi.org/10.1016/j.nimb.2012.02.009, 2013.

Wenger, A., Pugsley, K., O'Doherty, S., Rigby, M., Manning, A. J., Lunt, M. F., and White, E. D.: Atmospheric radiocarbon measurements to quantify CO_2 emissions in the UK from 2014 to 2015, Atmos. Chem. Phys., 19, 14057–14070, https://doi.org/10.5194/acp-19-14057-2019, 2019.

Yim, M.-S. and Caron, F.: Life cycle and management of carbon-14 from nuclear power generation, Progress in Nuclear Energy, 48, 2–36, https://doi.org/10.1016/j.pnucene.2005.04.002, 2006.

Zazzeri, G., Acuña Yeomans, E., and Graven, H. D.: Global and Regional Emissions of Radiocarbon from Nuclear Power Plants from 1972 to 2016, Radiocarbon, 60, 1067–1081, https://doi.org/10.1017/RDC.2018.42, 2018.

Zazzeri, G., Graven, H., Xu, X., Saboya, E., Blyth, L., Manning, A. J., Chawner, H., Wu, D., and Hammer, S.: Radiocarbon Measurements Reveal Underestimated Fossil CH_4 and CO_2 Emissions in London, Geophysical Research Letters, 50, e2023GL103834, https://doi.org/10.1029/2023GL103834, 2023.